Chapter 1

Introduction

Since the first implementation of a Laser system by Maiman [1] in 1960, there has been immense technological advancements in the field in the past sixty years. With the introduction of the path-breaking Chirped-Pulse Amplification (CPA)[2] technique, production of amplified femto-second duration pulses with petawatts of power have become a reality. When these high-intensity lasers are made to interact with any material, ionization of the material occurs almost instantly forming plasma. The plasma generated by the laser field can sustain high electromagnetic fields and is a rich area for many physical mechanisms. With the use of very high intensity lasers, any plasma electron in the laser field in a single laser period acquires velocity close to the velocity of light. The relativistic limit for electrons are exceeded with lasers of peak intensity, $I_0 \sim 10^{18} - 10^{23} W cm^{-2}$*. Led by the particle-driving potential of these high-powered lasers, a diverse new field- "laser-driven particle acceleration" emerged and flourished in the recent years. These advanced particle accelerators which uses an ultra-short, ultra-intense laser pulse interacting with a plasma, stands as a potent alternative to conventional radio-frequency oscillators such as linear accelerators (Linacs), cyclotrons, synchrotron etc. The maximum acceleration gradient achieved using a linac is of the order of* MeV/m*, compared to* $MeV/\mu m$ *[3] accelerating gradients provided by a picosecond pulsed intense laser pulse in plasma [4, 5, 6, 7, 8]. A room-sized (few metres), state-of the art laser system thus immensely cut down the size of the accelerator system, which is a huge advantage over kilometres-long standard particle accelerators. Apart from the generation of high energetic particle beams, the study of matter in presence of an intense laser field and the motion of the particles has led to the generation of x-ray free-electron lasers (x-FELs) [9, 10, 11], spontaneous*

magnetic field formation [12, 13], high harmonic generation [14, 15, 16], several instabilities and non-linear structure formation [17, 18], etc.

1.1 An overview on laser-driven particle accelerators

The concept of plasma-based particle acceleration was introduced by Vladimir Veksler in 1957 [19] even before the creation of laser. Tajima and Dawson [20], thereafter, proposed the first idea of a laser-based electron accelerator where the electromagnetic field of the laser drives a plasma wakefield that traps electrons and drive them to high energies. The motivation behind the innovative idea to utilise the extraordinary properties of lasers and plasma to accelerate particles comes from certain limitations of conventional particle acceleration mechanisms. The breakdown voltage of about $100MV/m$ requires the Linacs to have massive kilometre-long beam-lines. The huge manufacturing and maintenance cost limits its application in the somewhat lower (sub-GeV) energy sector. As the plasma is not limited by any breakdown voltage, extremely high accelerating gradients could be achieved in plasma in a much smaller region. It has been found that gradients of several TV/m [3] could be achieved in plasma which accelerates electrons to several GeVs of energies and protons to several MeVs of energies.

The electrons can directly acquire energy from the presently available intense lasers, however, ions, due to their higher masses usually depend on the electron motion to get accelerated. The laser intensity at present is not enough to directly drive ions to relativistic speeds. The strong quasi-static charge separation field created due to the displacement of the relativistic electrons causes the ions to dash along the direction of electron motion. The first experimental observation of multi-MeV protons using solid targets of few micron thickness was made independently by three groups in the year 2000 [21, 22, 23]. Special attention was garnered by Snavely, et al. [23] where 58 MeV protons were produced from

the rear-side (opposite to the laser-irradiated side) of the target in a well collimated manner. They used a wedge shaped target with the flat surface getting exposed to the laser pulse and found two beams of protons emitting perpendicular to the two rear edges. The theoretical explanation of the process was given by Wilks, et al. [24] in 2001 by introducing the model of Target Normal Sheath Acceleration (TNSA), where the protons are accelerated along a direction normal to the surface of the target rear-side. In TNSA, the electrons heated up by the laser pulse travel through the target length and form a negatively charged sheath near the rear surface of the target. The ions (predominantly the protons present as impurities) are accelerated from the target bulk towards the rear-side sheath to restore the charge neutrality. This mechanism is the most well-researched and well-understood way of accelerating ions till date although having certain shortcomings like, low energy scaling and broad energy spectra. Additionally there are several other acceleration processes like the Radiation Pressure Acceleration, Shockwave Acceleration, Coulomb Explosion etc. to name a few. A detailed discussion on each will be made in the upcoming sections of the chapter.

All the studied mechanisms of accelerating ions fall short in attaining a desirable energetic ion beam having all-round beam properties. These ion acceleration schemes require further improvements in terms of beam energy and flux. To attain these goals, the target and laser parameters are extensively tuned. It is found that the ion beam characteristics depend on the laser and target parameters immensely and in a complicated manner. Laser-driven ion acceleration has been proven to be a fertile and growing field of research that requires further studies and optimization for the cultivation of the energetic ions in certain applications.

1.2 Current and prospective applications of laser-driven ions

Several application sectors can get benefited by the inclusion of laser-driven energetic ions because of their easy accessibility and high tun-

ability. Some of such applications which can utilise such ion-beams are discussed below:

Hadron therapy

One of the most fantastic features of protons of MeV strength is their ability to deposit a large amount of the energy at the end of their path inside matter. When a fast moving charged particle travels inside matter it loses its energy to the surrounding material via collisions. The collision cross-section is inversely proportional to the energy of the particle, which reaches a peak at a certain distance in its path. This peak is known as the Bragg peak. Unlike electrons and gamma radiations, for ions, the Bragg peak is located at the end of their path making an ion beam suitable in tumour therapy [25] [Fig.1.1]. The localized treatment using protons and heavier ions reduces the collateral damages to healthy surrounding tissues in a significant manner. Depending on the site, size and stage of development of the cancerous growth, an ion beam of suitable initial energy can be administered to the patient requiring radiation treatment. Fig 1.2 shows the use of ion beams instead of conventional radiations in the treatment of malignant growth.

Such hadron therapies has now been successfully performed mostly with protons and carbon ions to patients in many countries across the globe. The conventional hadron therapy centres require cyclotrons or synchotrons for the acceleration of the ions. These ions are directed in beamlines with huge magnets to the treatment centre. These are then bent at appropriate angles using a large gantry depending upon the location of the cancer in the patient's body. The bulky accelerator system and the extensive beamline infrastructure has a very high installation and maintenance cost (exceeding 100M USD) which makes the treatment very expensive for the patients.

Laser plasma accelerated ions has the potential to reduce the issue of high cost because of its compressed size [28, 29, 30, 31]. The laser parameters could be easily tuned to adjust to the requirements of a particular patient. The ion source can also be varied which makes the en-

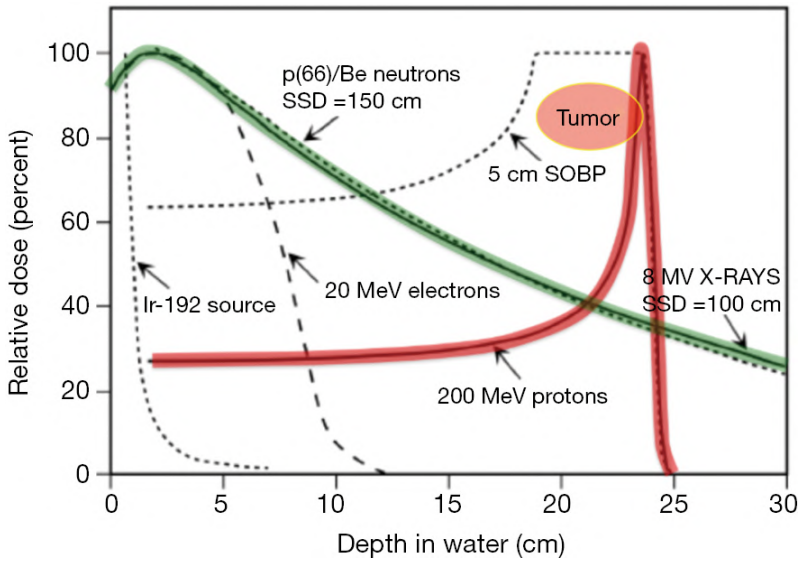

Figure 1.1: Dose deposition curve for X-rays, electrons, neutrons, and ions. The electrons, neutrons and X-rays have a continuous curve with high energy deposition outside of the targeted tumour region. The Bragg peak of the ion can be adjusted by varying the initial energy of the beam. For a larger target area the ions of different energies are modulated to form the Spread-out Bragg peak (SOBP) [26]

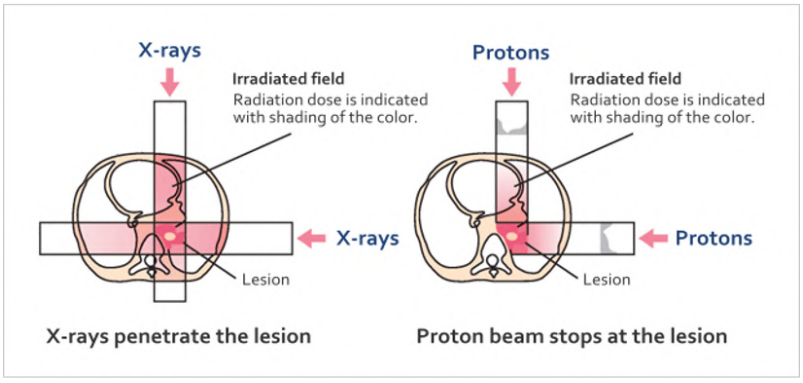

Figure 1.2: Radiation-therapy versus proton-therapy: The X-rays penetrate the tissue and deposit their energy continuously along the path. In contrast, a proton beam can be subjected to a localized region inside the body to destroy the malignant cells with a high precision. The healthy surrounding tissue gets minimally affected. The colour intensity represents the strength of the dose deposition. [27]

tire system highly customisable. Moreover, the laser beam can be guided using mirrors which may significantly reduce the use of bulky magnets and complex gantry systems. These factors provide an upper hand to these plasma-based accelerators over the conventional ones leading to an increased interest on these alternate acceleration studies among the research community. The affordability and the degree of precision that

could be provided by these laser-acceleration based therapy centres can greatly help mankind in its fight against cancer. However, these laser-based ion sources are still in the basic level of research, far from reaching the medical centres on a commercial platform. This is mainly because of the high energy spread and low energy of the ion beams than that required for medical treatment. The treatment of a deep-lying tumour inside the human body requires mono-energetic (energy spread $\leq 5\%$) protons of energy ~ 250 MeV or carbon ions of energy ~ 400 MeV. Moreover, to properly destroy the cancerous cells, a dose of $2 - 10$ Gy (1 Gy $= 1$ J/kg) in a few minutes is essential. This means a dose consisting of $\sim 10^{10}$ protons per second of energy ~ 250 MeV is required. Although at present such a high number of protons can be generated in a single shot, the repetition rate of most high power laser system is much lower than the requirement. Therefore, the broad (almost 100%) energy spread and low ion energies along with the low repetition rate of the lasers are the major hindrances that need to be addressed for the laser-driven ion beams to be commercially applicable in cancer therapy.

Proton radiography

The spatial and temporal resolution of the laser-accelerated proton beams make them a fine agent for proton probing. Reported in 1968, it was found that with a proton beam of range equal to the thickness of the object, a high contrast radiographic film can be generated [32]. The individual protons act like point sources and any object placed in front of these sources are probed to form images of high resolution. This technique can be utilised for the detection of electric and magnetic fields inside the plasma by tracing the deflections of the proton beams [33, 34, 35, 36]. The differential attenuation or scattering of the ion beam inside the target sample helps in the evaluation of its areal density. The detector system coupled with radio-chromic films (RCFs) or CR39 determines the energy range of the probe beam using the spatial intensity distribution on each layer. The energy spread also enables a multi-frame capacity to the imaging technique. As the target sample is

located at a finite distance from the probing source, a difference in the proton energy results in a difference in their time of arrival at the sample. Each layer of the detector stack retains information of individual times of the protons hitting the sample. Therefore, the imaging can be temporally resolved with discretized time frames. A typical schematic of the proton radiography set-up from laser-accelerated protons is shown in Fig. 1.3(a). The second laser (CPA_2) hits the proton target and causes the protons to accelerate and emit in the form of a beam. The emitted proton beam then probes the plasma that is created by the first laser pulse (CPA_1). The stack of RCF records the electric field evolution in time and generates the multi-frame image depending on the energy of the emitted protons.

Compared to conventional proton sources, laser-plasma sources are bet-

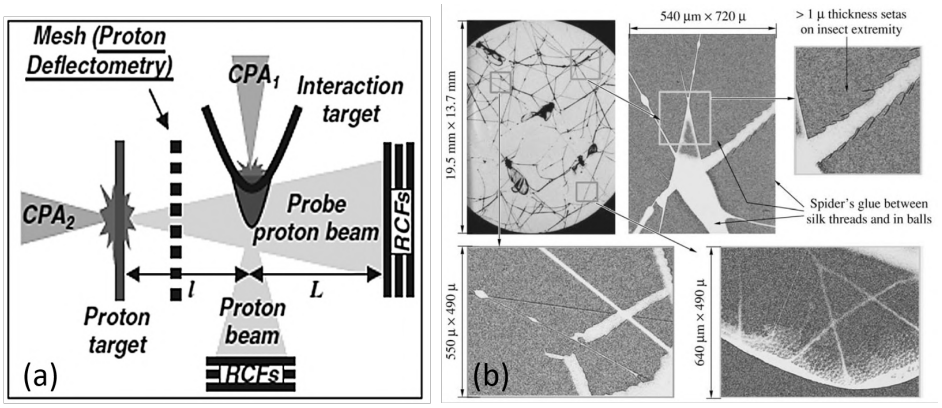

Figure 1.3: (a) A schematic of the experimental set-up of the proton radiography technique using lasers-plasma interaction [37]. (b) Ionographic image of a spider web with insects attached. The web hairs of width smaller than $1\mu m$ are resolved [38].

ter at resolving small objects with excellent sensitivity whose sizes are of the order of the attenuation length of the proton kinetic energy. Fig 1.3(b) shows the ionography images of a spider web where the different structures are visible with resolutions less than $1\mu m$ [38].

Generation of warm dense matter

The studies on extreme states of matter mimicking the stellar environment is of great interest for unravelling the mysteries of space and astrophysics. Such states having immensely high temperatures and densi-

ties break through the known regimes of both condensed matter physics and weakly coupled plasma physics. Such exotic matter has relevance in the context of fusion processes. The warm dense matter (WDM) is created by uniformly heating a solid material of large volume. Due to the high density of the target, lasers can penetrate and heat it only upto the skin depth making it unsuitable for the creation of WDM. On the contrary, ion beams have a penetration length and their Bragg peak at a larger depth inside the target helps in a much stronger volumetric heating. It is important to keep the duration of heating below the time scale of a significant hydrodynamic expansion. Hence the heating process is termed as 'isochoric heating'. Conventionally-accelerated ion beams have a notoriously high beam pulse duration which causes a premature expansion of the target without reaching the chosen temperature. The short pulse duration of the laser-accelerated ions serve beneficial in uniformly heating the target material without causing significant target expansion. A focused ion beam was reported to produce a warm dense plasma state of volume $500\mu m^3$ having temperature higher than 20 eV [39].

Fast ignition of fusion fuel

One of the methods to achieve fast ignition of fusion fuel is the inertial confinement fusion (ICF) where the Deuterium-Tritium (DT) fuel is compressed to ultra high densities ($10^{26} cm^{-3}$). The extreme compression ignites the centre of the fuel to high temperatures so that the Coulomb barrier is penetrated and the deuterium and tritium atoms can fuse to form helium atoms and release a substantial amount of energy (17.6 MeV). A degree of symmetry is essential to uniformly compress and reach a stage of ignition in the micron-sized spherical fusion pellet. A way of relaxing this stringent condition is a mechanism called 'fast ignition'. Here, the fusion pellet is first compressed using a bunch of synchronized high power laser. Thereafter, a burst of energy wave is made to hit the pre-compressed fuel which ignites and starts fusion reaction at the centre. Laser-accelerated particles could provide the energy boost required to initiate the fusion conditions [40, 41, 42]. Electrons

driven by a second intense and short laser pulse hits after the symmetrical compression of the pellet. However, the near-exponential energy deposition curve of the electrons make it difficult to focus the energy at a fixed spot to attain ignition. Protons on the other hand are capable of getting rid of this obstacle due to their localised Bragg peak, and were therefore proposed as an alternative fast ignitor [43]. Laser-driven protons of energy in the MeV range are focused on the hot point of the fuel to attain temperatures required for fusion. The temporal dispersion of the proton beam has been shown to enhance the heating of the fuel core [44, 45]. Apart from protons, other massive ions (especially carbon ions) have also shown increased efficiency as an ignitor in the fast ignition scheme [46, 47]. The requirement to use laser-driven ions as a fast ignitor for a standard pellet size is that the beam should be monoenergetic with an energy spread $\frac{\Delta\varepsilon}{\varepsilon} < 10\%$ with proton energy around $10 - 30$ MeV and carbon energy ~ 450 MeV. A schematic of the fast ignition arrangement is shown in Fig. 1.4.

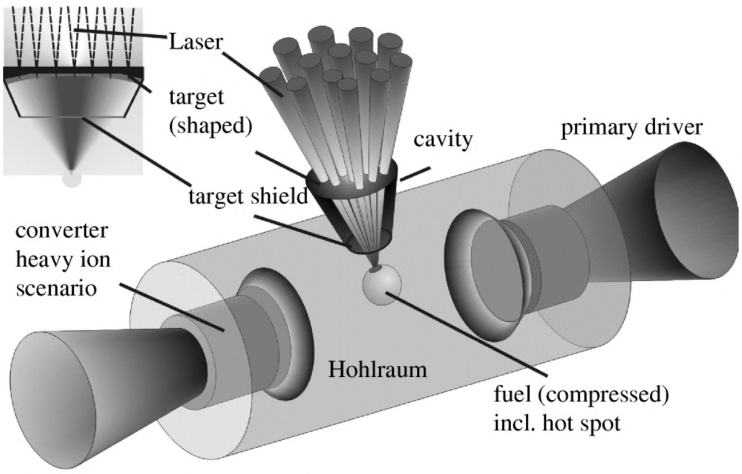

Figure 1.4: Fast ignition of fusion fuel using laser accelerated proton beam. The proton beam is focused on the compressed pellet using a shaped laser target [43].

1.3 Electromagnetic waves in Plasma

Plasma as a state of matter comprises of charged particles (both positive and negative), with their motions governed by the long-ranged self-

consistent electrostatic force between the components [48]. A plasma state is achieved in presence of extremely high temperatures or electric fields. Therefore, the irradiation of a super-intense laser field immediately ionises the target material and create plasma. The ionization threshold of the target material is very low compared to the peak intensity of the laser pulse and as a result the target is transformed to a plasma state even before the laser peak hits it.

The laser, essentially being an intense electromagnetic wave, is governed by the Maxwell's equations, (in cgs system)

$$\vec{\nabla}.\vec{D} = 4\pi\rho \tag{1.1}$$

$$\vec{\nabla}.\vec{B} = 0 \tag{1.2}$$

$$\vec{\nabla} \times \vec{E} = -\frac{1}{c}\frac{\partial \vec{B}}{\partial t} \tag{1.3}$$

$$\vec{\nabla} \times \vec{B} = \frac{4\pi}{c}\vec{J} + \frac{1}{c}\frac{\partial \vec{E}}{\partial t} \tag{1.4}$$

Here, $\vec{E}$ and $\vec{B}$ are the electric and magnetic fields; ρ and $\vec{J}$ are the charge and current densities respectively, and c is the velocity of electromagnetic wave in vacuum. $\vec{D}$ is the electric displacement vector and $\vec{D} = \vec{E}$ for a fully ionized propagating media.

The equation of the electromagnetic wave derived from the Maxwell's equations is thus given by,

$$\nabla^2\vec{E} - \vec{\nabla}(\vec{\nabla}.\vec{E}) = \frac{4\pi}{c^2}\frac{\partial \vec{J}}{\partial t} + \frac{1}{c^2}\frac{\partial^2 \vec{E}}{\partial t^2} \tag{1.5}$$

For a linear polarized wave of angular frequency ω and wave number k propagating along $\vec{z}$ with the polarization of the electric field along $\hat{x}$, the solution of the wave equation (1.5) is given by

$$\vec{E} = \hat{x}E_0 e^{-i(\omega t - kz)}, \tag{1.6}$$

$$\vec{B} = c\vec{k} \times \frac{\vec{E}}{\omega}, \tag{1.7}$$

$$\vec{k} \times \vec{E} = 0 \tag{1.8}$$

While the electromagnetic wave is propagating inside a plasma medium, the constituent charged particles of the medium (predominantly the electrons due to their high charge by mass ratio), starts responding to the electromagnetic field. The ions are considered immobile for this treatment as they have a much higher response time. The motion of an electron with mass m_e having velocity $\vec{v}$ is determined by the Lorentz force equation,

$$m_e \frac{d\vec{v}}{dt} = m_e \left[\frac{\partial \vec{v}}{\partial t} + \vec{v}(\vec{\nabla}.\vec{v}) \right] = -e \left[\vec{E} + \frac{1}{c}(\vec{v} \times \vec{B}) \right] \tag{1.9}$$

For weak electric fields, the electron velocity is significantly low and the second-order terms in the force equation ($\vec{v}(\vec{\nabla}.\vec{v}$ and $\vec{v} \times \vec{B}$)can be neglected. Thus,

$$\frac{\partial \vec{v}}{\partial t} = -\frac{e}{m_e}\vec{E} \tag{1.10}$$

Thus the current density of the electrons in the plasma medium of density n_0 will be,

$$\vec{J} = -en_0\vec{v} \tag{1.11}$$

and

$$\frac{\partial \vec{J}}{\partial t} = -en_0 \frac{\partial \vec{v}}{\partial t} = \frac{n_0 e^2}{m_e}\vec{E} \tag{1.12}$$

The above equation can be re-written using the electron plasma oscillation frequency $\omega_{pe} = \sqrt{\frac{4\pi n_0 e^2}{m_e}}$ as

$$\frac{\partial \vec{J}}{\partial t} = \frac{\omega_{pe}^2}{4\pi}\vec{E} \tag{1.13}$$

Using equation (1.6), the above equation becomes,

$$\vec{J} = \frac{i\omega_{pe}^2}{4\pi\omega}\vec{E} = \sigma\vec{E} \tag{1.14}$$

Here, $\sigma = \frac{i\omega_{pe}^2}{4\pi\omega}$ is the plasma high-frequency conductivity. To deduce the dispersion relation of an electromagnetic wave of frequency ω inside a uniform plasma medium ($\vec{\nabla}.\vec{E} = 0$) of electron plasma frequency ω_{pe},

equation (1.12) is substituted in equation (1.5) and using equation (1.6),

$$\omega^2 = \omega_{pe}^2 + k^2c^2 \tag{1.15}$$

The dispersion relation states that the propagation of the electromagnetic wave ($k^2 > 0$) inside the plasma medium occurs only if $\omega > \omega_{pe}$. On the contrary, if $\omega < \omega_{pe}$, the electrons obtain enough time to respond and shield the fields of the incident wave. As a result, the wave becomes evanescent ($k^2 < 0$) and the energy gets absorbed inside such a plasma medium [49]. The electric field exponentially decays inside the medium and the characteristic length is called the collisionless skin-depth $\delta_s = c/\omega_{pe}$. These two conditions define a limiting criterion where $\vec{k} = 0$ i.e. $\omega = \omega_{pe}$. This condition is fulfilled when the plasma density is of a critical value termed as 'critical density', $n_c = \dfrac{m_e\omega^2}{4\pi e^2}$. Thus, when a plasma has density greater than the critical density, the wave gets absorbed inside the medium and the plasma is termed as 'overdense'. Conversely, the incident wave propagates inside an 'underdense' plasma with density less than the critical density. The critical density is obtained for a plasma when its density becomes equal to $(1.11 \times 10^{21}\lambda_{\mu m}^{-2})cm^{-3}$, where $\lambda_{\mu m}$ is the wavelength of the incident wave in micrometres. The propagation or absorption of the electromagnetic wave inside the plasma is determined by the electron-plasma frequency and the refractive index of the plasma for a wave of frequency ω is $\eta \simeq \sqrt{1 - \dfrac{\omega_{pe}^2}{\omega^2}}$.

1.3.1 Single electron interaction with a laser field

For a simplified understanding, the impact of the laser field on a single electron is considered [50]. A plane polarized wave will have

$$\vec{E}(\vec{z}, t) = E_0 e^{-i(\omega t - kz)}\hat{\zeta} \tag{1.16}$$

where, $\hat{\zeta}$ is a complex polarization vector. For linear polarization, $\hat{\zeta} = \hat{x}$ and for circular polarization, $\hat{\zeta} = \dfrac{1}{\sqrt{2}}(\hat{x} \pm \hat{y})$. Considering weak electric field strengths, $v \ll c$ and thus the second order term in the Lorentz

force equation may be neglected. Solving the equation,

$$\vec{v} = -\frac{ie}{m_e\omega}\vec{E} \Rightarrow \vec{r} = \frac{e}{m_e\omega^2}\vec{E} \tag{1.17}$$

For linear polarization, the electron trajectory is a straight line along the direction of polarization, and for circular polarization, it is a circle in the x-y plane. To represent the threshold where the non-linear effects start appearing, a dimensionless parameter is defined, viz, the laser strength parameter, a_0, which is the ratio of the maximum quiver velocity of the electron to the velocity of light in vacuum,

$$a_0 = \frac{eE_0}{m_e\omega c} \tag{1.18}$$

For lasers with $a_0 < 1$, the electron motion remains non-relativistic, whereas for lasers with $a_0 > 1$ the non-linear terms start contributing and the electron motion becomes relativistic. In practical terms, a_0 can be defined as

$$a_0 = 0.85\left(\frac{I_0\lambda_{\mu m}^2}{10^{18}Wcm^{-2}}\right) \tag{1.19}$$

For lasers with $a_0 > 1$ corresponding to peak laser intensity $I_0 > 1.37 \times 10^{18}Wcm^{-2}$, the magnetic field is strong enough to start contributing in the electron motion. The electron velocity becomes relativistic and the Lorentz relativistic factor $\gamma = \sqrt{1 + \frac{a_0^2}{2}}$ becomes significantly high. The solution to the electron trajectory now require the fully non-linear treatment. Considering the wave with vector potential,

$$\vec{A} = A_0[\hat{x}\varsigma cos\phi + \hat{y}(1-\varsigma^2)^{1/2}sin\phi] \tag{1.20}$$

Where, $\phi = (kz - \omega t)$ and $\varsigma \leq 1$ defines the polarization of the incident wave so that $\varsigma = 1$ or 0 corresponds to linear polarization along $\hat{x}$ or $\hat{y}$ respectively. For circular polarization, $\varsigma = \pm\frac{1}{\sqrt{2}}$. Solving the equation of

motion, the trajectory of the electron can be obtained implicitly as

$$\hat{x} = -\varsigma a_0 sin\phi \tag{1.21}$$

$$\hat{y} = a_0(1-\varsigma^2)^{1/2} cos\phi \tag{1.22}$$

$$\hat{z} = \frac{a_0^2}{4}\left[-\phi - \left(\varsigma^2 - \frac{1}{2}\right) sin2\phi\right] \tag{1.23}$$

As a result, for a linearly polarized case, the electron motion will be

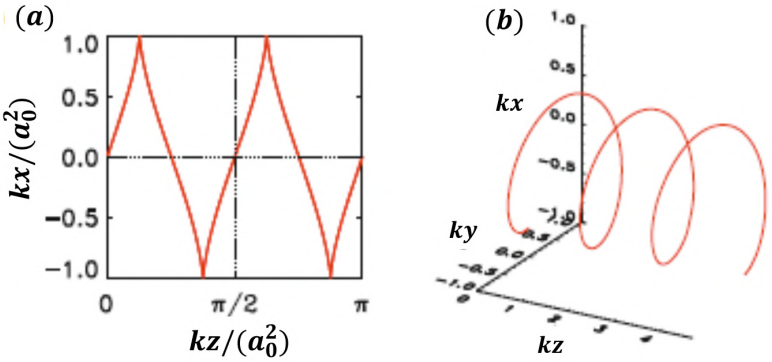

Figure 1.5: (a) Electron trajectory in a single-frequency plane-polarized wave of dimensionless amplitude a_0. (b) The electron trajectory in a presence of a circularly polarized wave of $a_0 = 2$. (Adapted from [50])

oscillatory along the polarization direction. In the longitudinal direction, there is a superposition of oscillatory motion at twice the laser-frequency and a drift motion along the propagation direction. For higher laser amplitudes ($a_0 \gg 1$), the magnetic field dominates the electron motion and linear term in ϕ give rise to an effective displacement of the electron in the longitudinal direction with a drift velocity given by $v_d = \frac{ca_0^2}{a_0^2+4}$. The longitudinal drift motion along with the transverse oscillatory motion results in a figure-8 pattern in the electron frame of reference. The electron motion in presence of such relativistic fields is shown in Fig 1.5. For circularly polarized lasers, the electron attains a longitudinal drift along the otherwise transversely circular motion. This results in a helical trajectory with a longitudinal axis having radius $R_c = \frac{a_0}{\sqrt{2}k} = \frac{a_0\lambda}{2\sqrt{2}\pi}$ in the x-y plane. For a continuous laser, an electron in vacuum does not gain any energy from the laser as the amount of energy gained is immediately reverted back to the field as the laser passes (the Lawson-Woodward

theorem). However, this "no-acceleration" theorem can be avoided by the use of a focused, short envelop of laser field. Such laser pulsed may help the electron to de-phase from the laser field. Now, when the laser is stopped in its course as it reached the critical layer of the plasma medium, the excited electron may propagate uninhibited inside the plasma attaining the energy from the laser pulse. Such focused lasers may generate electrons with MeVs of energies in a single optical cycle.

1.4 Ponderomotive force and potential

In reality, the laser used for the interaction studies are not continuous and perfectly monochromatic, and are rather spread out in both space and time as small bunches of strong electromagnetic radiations. Such packages or pulses help in setting up a finite motion of the interacting electrons. These laser pulses have variations in the intensities both spatially (i.e. along the directions perpendicular to the laser motion) and temporally (i.e. along the laser propagation direction). The spread in the transverse and longitudinal directions define two important parameters of the laser, viz, the spot size and the temporal pulse duration respectively. Usually, a laser pulse has a Gaussian shape both spatially and temporally and these parameters are defined by the full-width at half-maxima (FWHM) of the corresponding spatial and temporal spreads. These types of variations in the intensities of the laser give rise to a non-linear force known as the 'Ponderomotive force' which explicitly arises due to the interaction of an electron with an inhomogeneous electromagnetic field.
For an electromagnetic wave having a spatial variation in the electric field, $\vec{E} = \vec{E_s}(\vec{r})cos\omega t$. Solving the Lorentz force equation, for an initial position r_0,

$$\vec{v_1} = -\frac{e}{m_e\omega}\vec{E_s}sin\omega t \tag{1.24}$$

$$\delta\vec{r_1} = \frac{e}{m_e\omega^2}\vec{E_s}cos\omega t \tag{1.25}$$

The $\vec{v} \times \vec{B}$ in the first order becomes zero because both the vectors individually vanish at equillibrium, leaving the first order values $\vec{v_1}$, $\vec{B_1}$ and $\vec{r_1}$. Now, expanding $\vec{E}(\vec{r})$ about r_0,

$$\vec{E}(\vec{r}) = \vec{E}(\vec{r_0}) + (\delta\vec{r_1}.\vec{\nabla})\vec{E}|_{\vec{r}=\vec{r_0}} + ... \tag{1.26}$$

The second order part of the Lorentz force equation may be written as

$$m_e \frac{d\vec{v_2}}{dt} = -e\left[(\delta\vec{r_1}.\vec{\nabla})\vec{E} + \frac{\vec{v_1} \times \vec{B_1}}{c}\right] \tag{1.27}$$

Using Maxwell's law to obtain the value of $\vec{B_1}$,

$$\vec{B_1} = -\frac{c}{\omega}\vec{\nabla} \times \vec{E_s}|_{\vec{r}=\vec{r_0}} sin\omega t \tag{1.28}$$

Substituting these values in equation [1.27] and taking the time average,

$$m_e \left\langle \frac{d\vec{v_2}}{dt} \right\rangle = -\frac{e^2}{2m_e\omega^2}[(\vec{E_s}.\vec{\nabla})\vec{E_s} + \vec{E_s} \times (\vec{\nabla} \times \vec{E_s})] \tag{1.29}$$

Using the vector identity

$$\vec{E_s} \times (\vec{\nabla} \times \vec{E_s}) = \frac{1}{2}\vec{\nabla}E_s^2 - (\vec{E_s}.\vec{\nabla})\vec{E_s} \tag{1.30}$$

Thus, the time-averaged non-linear force on a single electron may be written as

$$\left\langle \vec{f_p} \right\rangle = m_e \left\langle \frac{d\vec{v_2}}{dt} \right\rangle = -\frac{e^2}{4m_e\omega^2}\vec{\nabla}\left\langle E_s^2 \right\rangle \tag{1.31}$$

The corresponding ponderomotive potential is given by

$$\Phi_p = \frac{e^2}{4m_e\omega^2}E_s^2 = \frac{m_e c^2}{4}a_0^2 \tag{1.32}$$

The cycled-average energy attained from the laser field by an oscillating electron is the quiver energy and is given by

$$k_B T_e = m_e c^2(\gamma - 1) = m_e c^2\left(\sqrt{1 + \frac{a_0^2}{2}} - 1\right) \tag{1.33}$$

The total force on the electrons per unit volume in a plasma of electron density n_e is

$$\vec{F_p} = n_e \left\langle \vec{f_p} \right\rangle = -\frac{\omega_p^2}{16\pi\omega^2} \vec{\nabla} \left\langle E_s^2 \right\rangle \tag{1.34}$$

The ponderomotive force becomes dominant as the laser intensity becomes relativistic. This force is proportional to the electron charge density and the gradient of the square of the electric field. Moreover it is directed opposite to the gradient of the electric field. As a consequence of this ponderomotive force, the electrons are expelled from regions of high field intensities. As this force is proportional to e^2, it is charge independent but the presence of the mass-term in the denominator makes its effect on heavier ions rather small. When the electrons are influenced by the ponderomotive force, their displacement creates a charge separation field $\vec{E_{cs}}$. Therefore, the total force experienced by the electrons,

$$\vec{F_e} = -e\vec{E_{cs}} + \vec{F_p} \tag{1.35}$$

Since $\vec{F_p}$ is small in case of ions, the total force experienced by the ions

$$\vec{F_i} = e\vec{E_{cs}} \tag{1.36}$$

Thus, the total force on the system

$$\vec{F_{total}} = \vec{F_p} \tag{1.37}$$

In case of a Gaussian shaped laser pulse, the gradient of the electric field is directed inwards and therefore, due to the effect of the ponderomotive force electrons are ejected out of the Gaussian pulse both in the transverse and longitudinal directions as seen in Fig 1.6.

The polarization of the laser determines the oscillation characteristic of the ponderomotive force. For linear polarization, $\vec{E} = \hat{x}\vec{E_s}(\vec{r})cos\omega t$. Therefore,

$$\vec{f}_{p,LP} = -\frac{e^2}{8m_e\omega^2} \vec{\nabla}[E_s^2(\vec{r})(1 + cos(2\omega t))] \tag{1.38}$$

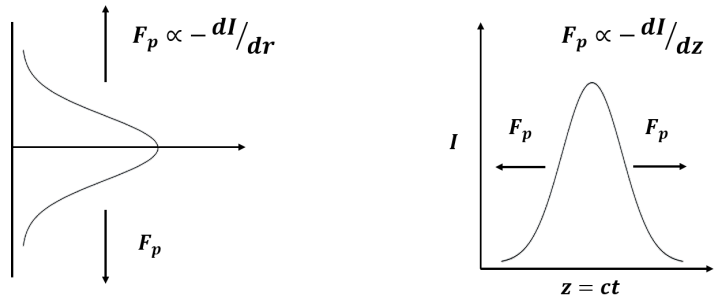

Figure 1.6: Ponderomotive force on electrons in presence of a Gaussian pulse. The electrons are ejected from the pulse centre both in the transverse and longitudinal directions.

And, for circular polarization, $\vec{E} = \frac{1}{\sqrt{2}}[\hat{x}\vec{E_s}(\vec{r})cos\omega t \pm \hat{y}\vec{E_s}(\vec{r})sin\omega t]$ and therefore,

$$\vec{f}_{p,CP} = -\frac{e^2}{4m_e\omega^2}\vec{\nabla}E_s^2(\vec{r}) \tag{1.39}$$

The ponderomotive force in the linear case consists of a slow varying steady component (the first term) and an oscillating component (second term) with frequency 2ω. On the other hand, the circularly polarized case consists of only a slow varying steady term.

1.5 Relativistic laser effects

When the field amplitudes of the laser are sufficiently high ($a_0 > 1$) and the electron motion becomes relativistic, the dispersion relation of an electromagnetic wave in a plasma medium (equation 1.15) gets modified to accommodate the relativistic correction in the electron mass as

$$\omega^2 = \omega\prime_{pe}^2 + k^2c^2 \tag{1.40}$$

Here, $\omega\prime_{pe} = \frac{\omega_{pe}}{\sqrt{\gamma}} = \sqrt{\frac{4\pi n_0 e^2}{\gamma m_e}}$ is the relativistically modified plasma frequency. Therefore in the relativistic case, the plasma frequency is reduced by a factor of $\sqrt{\gamma}$, but since γ is dependent on a_0, the cycled-average value $\gamma = \sqrt{1 + \frac{a_0^2}{2}}$ is considered. Correspondingly, the critical density is also modified as $n_{cr} = \gamma n_c$. Thus for relativistic laser in-

tensities, the critical density layer gets shifted towards higher density and the intense laser can penetrate for a longer distance in a plasma medium of increasing density. This effect of intense laser is termed as the 'relativistically-induced transparency'. The relativistic correction modifies the optical properties of the plasma medium through the alteration of the refractive index given by $\eta = \sqrt{1 - \frac{\omega_{pe}^2}{\omega^2}}$. With a Gaussian-like spatial variation in the laser intensity profile where the intensity is peaked at the axis $(r = 0)$, then $\gamma(r = 0) > \gamma(r > 0)$. As a result, the $\eta(r)$ will have a maximum on axis. The phase velocity will thus have a spatial variation, with the wave travelling slower where intensity is higher (high a_0) leading to an inward curvature in the laser wave-front, causing the laser to converge. The spatial variation in the laser intensity results in the optical guiding of the laser and this phenomena is known as the 'relativistic self-focusing'. The threshold power above which the self-focusing effect occurs is given by $P_c = 17\left(\frac{n_c}{n_e}\right) GW$. The focusing effect continues till it reaches the diffraction limit of the laser. The self-focusing phenomena consequently leads to self modification of the spatial and temporal profiles of the laser inside the plasma medium. As discussed in the previous section, the use of a Gaussian shaped pulsed laser ejects out the electrons radially from the laser centre by the action of the ponderomotive force. The electron evacuation process ultimately effects the ion motion due to the charge-separation field. This creates a density drop on the axis $[n_e(r = 0) < n_e(r > 0)]$. As a result, the refractive index at the axis will get modified which will lead to the focusing of any trailing pulse propagating inside the medium. This 'ponderomotive self-focusing' enhances the effect of the self-focusing induced due to relativistic fields of the laser.

1.6 Ultrashort intense laser pulses

The generation of intense ultra-short pulse was an extremely challenging job before the invention of the Chirped Pulse Amplification (CPA) technique by Mourou and Strickland [2]. As the laser intensity (I_0) is in-

versely proportional to the laser pulse duration (τ), compressing the laser pulse beyond the nanosecond limit using cascaded amplifiers makes the peak intensities extremely high. As a result, the non-linear portion of the refractive index becomes significantly high which leads to non-linear effects like self-focusing and damages the optical medium. The introduction of CPA helped in getting rid of these issues and compressed femtosecond pulses having peak power of the order of petawatts could be generated. In CPA-laser systems, an ultrashort laser pulse of moderate intensity is first stretched temporally and then amplified to the targeted intensity, before compressing it back to achieve an ultrashort pulse of high intensity. Although seemingly simple, the proper implementation of a CPA procedure is full of challenges. The compressibility of the pulse is limited by the material damage threshold of the pulse compressor grating which is subjected to extremely high energetic laser beams. Although it is a widely known concept that a laser is a coherent, monochromatic beam of electromagnetic radiation, any laser pulse as a matter of fact has a finite frequency bandwidth. The pulse duration (τ) is dependent on the bandwidth ($\Delta\omega$) of the laser gain media as $\tau \geq \frac{k}{\Delta\omega}$, where the constant k is dependent on the shape of the pulse. For a Gaussian pulse with temporal profile $\propto e^{-(t/\tau)^2}$, $\tau\Delta\omega \sim 1$. Therefore an extremely short pulse will have a broad bandwidth.

The existence of the finite temporal spread in the pulse causes the target to encounter irradiances starting from zero to the peak value as the laser propagates. A clean Gaussian ultrashort pulse is realistically difficult to obtain. The presence of any structure in the intensity profile at a earlier time before the arrival of the peak laser can ignite the solid target at the interaction region and create plasma. Such structures are referred to as 'pre-pulses' and are often caused by the amplified spontaneous emission (ASE) of the amplifiers or due to leakage from Pockel cells and may spread out upto nanoseconds in time. These prepulses are advantageous where target heating is essential and facilitates efficient generation of hot electrons. The prepulses also aids the production of x-rays. However, their presence has a negative impact in those cases where keeping the

solid target intact is crucial. For such cases, the prepulse intensity must be kept below the ionization threshold of the target material to avoid plasma production in the interaction site before the arrival of the pulse peak. The intensity of the ASE is defined by a term known as the contrast ratio which is the ratio of the peak pulse to the ASE intensity. A high contrast ratio laser pulse is used to prevent the production of the preplasma. A typical temporal profile of an intense ultrashort pulse is shown in Fig 1.7.

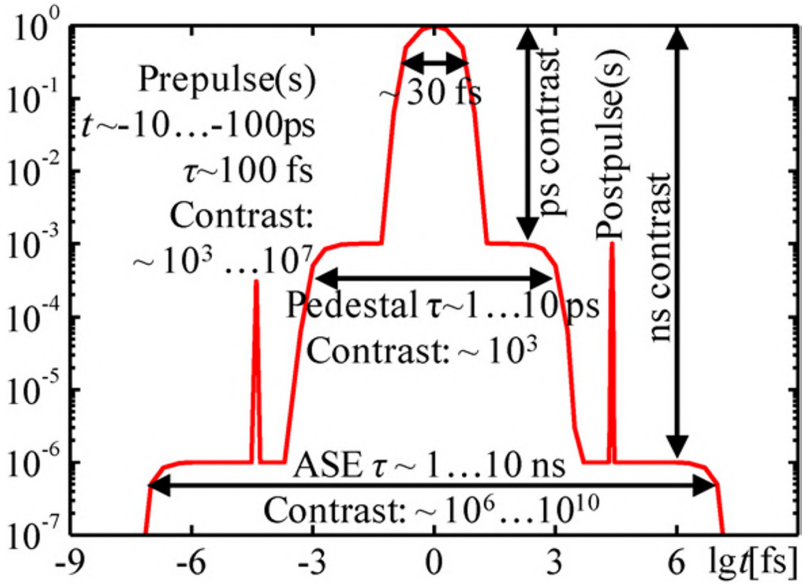

Figure 1.7: Typical temporal profile of an intense ultrashort laser pulse. Figure taken from [51].

1.7 Laser absorption mechanisms in plasma

The propagation of the laser pulse stops upon reaching the critical density layer and a fraction of the laser energy is absorbed inside the plasma. The electrons, having the highest charge to mass ratio, responds quickly to the laser action and carries the absorbed energy from the laser thus heating the interaction region. These excited electrons are known as the hot or fast electrons. Using the currently available lasers, only electrons can be subjected to relativistic motion directly from the lasers. For protons, which have mass $m_p \approx 1868 m_e$, the laser intensities required

to set them in a relativistic oscillatory motion is about $5 \times 10^{24} W cm^{-2}$ for a laser of wavelength $1 \mu m$. This is much higher than the irradiances of currently available lasers ($10^{18} - 10^{22} W cm^{-2} \mu m^2$). There are several absorption mechanisms responsible for the transfer of energy from the laser pulse to the hot electrons. These mechanisms depend greatly on the laser intensity, polarization, pulse duration, angle of incidence, plasma density and scale length, etc.

1.7.1 Inverse bremsstrahlung heating

It is a collisional type of absorption mechanism and takes place in cases of low intensity laser pulse ($I_0 < 10^{15} W cm^{-}2$). The electrons interact with the laser field and start oscillating and in turn transfer momentum to the surrounding plasma ions due to collisions. The electron-ion collision frequency is given by $\nu_{ei} = \frac{Z n_e}{T_e^{3/2}}$ where Z is the degree of ionization of the plasma and T_e is the temperature of the excited electrons. The inverse bremsstrahlung effect is strong for low electron temperature. The number of collisions decreases as the electron energy increases and thus for higher laser intensities other collisionless methods starts governing the laser energy absorption into the plasma.

1.7.2 Resonance absorption

Resonance absorption occurs when a p-polarized laser (the polarization vector on the plane of incidence) of moderate intensity ($I \leq 10^{17} W cm^{-2}$) is obliquely incident on a plasma of long density scale length. It is a collisionless absorption mechanism where the laser energy directly couples with the plasma forming electron-plasma waves. The obliquely incident ($\theta > 0$) wave propagates inside the plasma with density gradient $\vec{\nabla} n_e$ until it reaches the critical density layer beyond which it gets reflected. However, due to the obliquity of the laser, the critical density layer gets modified to $n_c cos^2\theta$. At the point of reflection, the electric field has a direction parallel to the density gradient which cause the plasma electrons to oscillate at the laser frequency. The resonance condition ($\omega_p = \omega$) excite a strong electron plasma wave that carry the laser energy along the direction of plasma gradient. A schematic representation of the process

is shown in Fig. 1.8. This mechanism require large density scale lengths $L_s = \frac{n_e}{\vec{\nabla} n_e}$ because if the scale length is less than the plasma wave amplitude, electron will escape to the vacuum breaking the resonance. The plasma wave delivers the energy to the remaining plasma due to wave-breaking or by collisions. This type of absorption does not occur in case of s-polarized lasers (polarization vector perpendicular to the plane of incidence) as $\vec{E}.\vec{\nabla} n_e = 0$ and no density perturbation is created at the laser reflection site.

The component of the electric field driving the electron wave along the

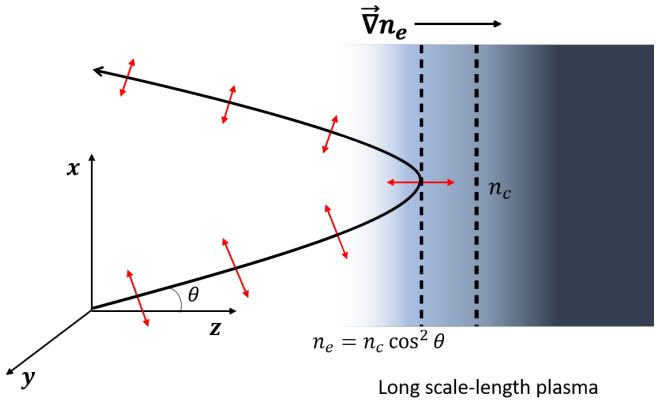

Figure 1.8: Schematic of resonance absorption of a p-polarized laser in long density gradient plasma

density gradient is obtained as [49]

$$\vec{E_d} = \frac{\vec{E}}{\sqrt{2\pi\omega L_s/c}} \phi(t') \tag{1.41}$$

Here, $\phi(t') \simeq 2.3 t' e^{-2t'^3/3}$ and $t' = \left(\frac{\omega L_s}{c}\right)^{1/3} sin\theta$. Thus, $\vec{E_d}$ vanishes as $t' \to 0$ which asserts that resonance absorption is suppressed as $L_s \to 0$ and $\theta \to 0$. However, $\vec{E_d}$ becomes negligible even for large values of t' where the laser field has to travel a large distance before reaching the critical density layer. An optimal condition of laser absorption is achieved when $\theta \approx sin^{-1}\left[0.8\left(\frac{c}{\omega L_s}\right)^{1/3}\right]$ [49].

Although resonance absorption is suppressed for higher laser intensities, its study is important due to the presence of the pre-pulses which have

the ability to produce plasma at the interaction region and isothermally expand the front side of the target creating a plasma gradient of large scale length.

1.7.3 Vacuum/Brunel heating

For steep density gradients ($L_s \ll \lambda$) in the plasma, where the electron-plasma wave amplitude is greater than the plasma scale-length, the vacuum heating has a significant contribution in the absorption of the laser pulse. This mechanism was developed by Brunel [52] (hence it is also known as Brunel heating) as the "not-so-resonant, resonant absorption". Brunel heating is an extension of the resonant absorption process that accommodates plasmas of shorter scale-length. Similar to the previous mechanism, the p-polarized laser is incident at an angle θ which sets up the electron oscillation at the reflecting surface. However, as the density scale length is less than the electron amplitude, the electron is pushed out of the plasma to the vacuum. In the meantime, inside the overdense plasma, the laser electric field amplitude decays exponentially with a skin-depth δ_s. The electron ejected out to the vacuum is then pulled back inside the plasma in the next half-cycle of the laser. However, as the laser field is evanescent at the overdense region, the electron can travel farther inside the plasma than the laser field. In this way the energetic electrons escape the restoring force of the laser field and propagate inside the target with a frequency $\omega_p \approx \omega$. The mechanism of vacuum heating is schematically shown in Fig 1.9.

1.7.4 $J \times B$ heating

The $\vec{J} \times \vec{B}$ heating becomes effective at relativistic laser intensities ($a_0 > 1$). This mechanism requires an almost step like density profile. The high value of the laser magnetic field $\vec{B}$ and the relativistic electron velocity makes the $\vec{v} \times \vec{B}$ term of the Lorentz force significantly high. Due to this term the electron displays an oscillating motion along the direction of the laser propagation with a frequency 2ω [from equation (1.23)] for a linearly polarized laser. In this mechanism, the electron motion is driven in the longitudinal direction by the magnetic field of the laser which

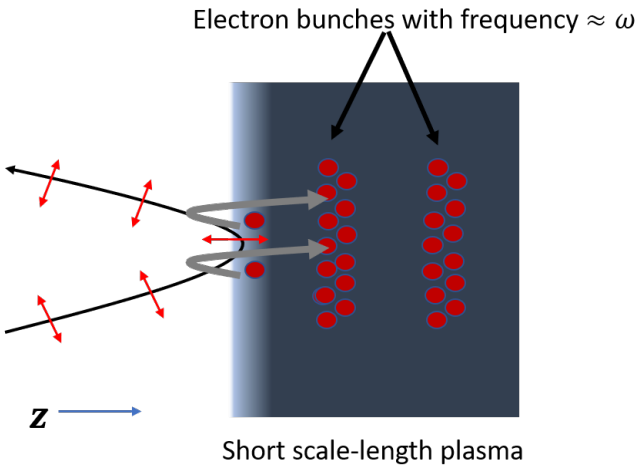

Figure 1.9: Schematic of vacuum/Brunel heating mechanism of a p-polarized laser in short density gradient plasma

is in contrast with the vacuum heating where the driving agent is the electric field. The $\vec{J} \times \vec{B}$ effect is most efficient at normal laser incidence. In case of circularly polarized laser, the oscillating component in the equation (1.23) vanishes and therefore the electrons are pushed inside the target in a steady manner. This mechanism of producing hot electrons is suppressed for circular polarized laser, and thus, circularly polarized lasers are used in the interaction studies where the target heating is required to be kept minimal.

1.8 Ion acceleration due to laser-plasma interactions

The basic concept of accelerating ions using intense lasers to MeV energies is by creating quasi-static electric fields high enough to pull protons and other heavy ions from the target. With the direct absorption of laser energy the fast electrons create the necessary charge separation field for the acceleration of the ions. With the presently available laser intensities electrons act as the medium for energy exchange between the laser and the eventual ions. Depending on the different laser and target conditions, a number of ion acceleration schemes have been identified and studied,

some more extensively than the others. Some of these ion acceleration mechanisms are discussed in the following sub-sections. Usually, two or more of these acceleration processes act together in synergy to yield the energetic ions. The dominant acceleration processes are crucially governed by the different laser and target parameters.

1.8.1 Target Normal Sheath Acceleration

As already mentioned in Section 1.1, this is the most widely-studied mechanism of accelerating ions using an intense laser pulse. Both simulations and experiments have shown that when an intense pulse of relativistic intensities ($I_0 > 10^{18} W cm^{-2}$, $a_0 \geq 1$) is incident on a micrometre thick foil target of solid density, the strong field of the rising edge of the pulse ionizes the interaction region at the laser-irradiated surface of the target and creates plasma. The laser pulse propagation is inhibited inside the overdense plasma and a portion of the laser energy is absorbed by the electrons creating a population of hot electrons. The energy of these hot electron can be given by the ponderomotive or Wilks' scaling [53] $k_B T_e = m_e c^2(\gamma - 1) = m_e c^2 \left(\sqrt{1 + \frac{a_0^2}{2}} - 1 \right)$. These hot electrons cross the target and escapes from the rear-side of the target. This creates a negatively charged sheath field at the target rear surface that extends upto a few Debye lengths $\lambda_{dh} = \sqrt{\frac{k_B T_h}{4\pi n_{eh}}}$. The strength of the sheath electric field is sufficient to ionize the target rear side which is $E_s \approx \frac{k_B T_h}{e \lambda_{dh}}$. The ions are pulled towards the target rear-side to neutralise the charge separation field. The protons that are usually present in the target either as target constituents or as impurities are favourably accelerated due to their higher charge by mass ratio, compared to other heavier ions. These ions (mostly protons) travel along a direction normal to the electrostatic sheath, hence providing the name Target Normal Sheath Acceleration. The ions are accelerated as long as there is the production of hot electrons and so the time-scale of acceleration is usually of the order of the laser pulse duration. The acceleration mechanism is shown in Fig. 1.10.

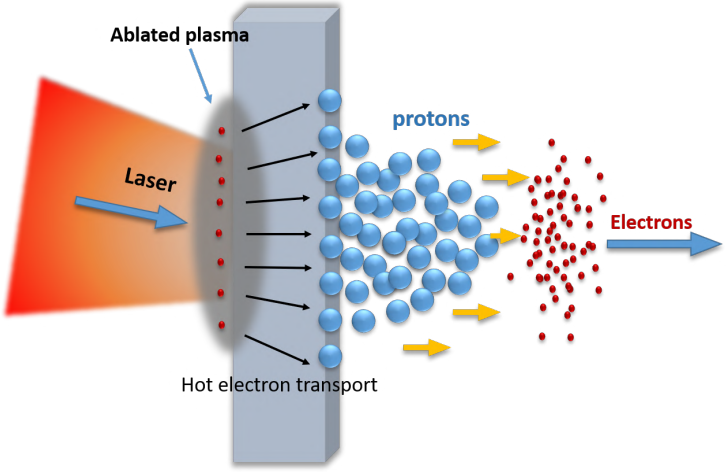

Figure 1.10: Schematic of the TNSA mechanism with the intense laser irradiating a solid target of micron sized thickness causing the generation of heated electrons that accelerates the protons (present as contaminants) normal to the negative sheath field.

In order to explain the acceleration mechanism and to provide a scaling of the proton energies several analytical and numerical models were proposed [24, 53, 54, 55, 56, 57]. The free expansion of plasma into vacuum was presented by Mora [57] using a 1D plasma model. The proton spectrum was predicted to be an exponentially decreasing one having a sharp cutoff value, given by

$$\varepsilon_{max} = 2Zk_BT_e[ln(\tau + \sqrt{\tau + 1})]^2 \tag{1.42}$$

Here, $\tau = \dfrac{\omega_{pi}t}{\sqrt{2e_N}}$, where $\omega_{pi} = \sqrt{\dfrac{4\pi Zn_{e0}e^2}{m_i}}$ is the ion-plasma frequency of ion mass m_i and $e_N = 2.71828....$ Here, Z is the degree of ionization and Zn_{e0} is the original ion density before expansion. Considering the acceleration time 't' to be high enough to ensure heating of the electrons by the laser pulse at the target front surface, the condition $\omega_{pi}t \gg 1$ is assumed to be true. Therefore, the cutoff energy can be calculated using $\varepsilon_{max} \simeq 2Zk_BT_e[ln(2\tau)]^2$. The acceleration time $t \sim 1.3\tau_L$ is found to provide a satisfactory prediction of the energy scaling as reported in [58]. Mora extended the plasma expansion model using thin targets in [59]. The model considers the adiabatic cooling of the electrons due to the transfer of energy to the ions which causes the co-existence of two-

temperature electron populations. The dependence of the ion energy on the target foil thickness provided by this model agrees with the experimental scenarios and introduce a limitation on the foil thickness. In another model to describe the TNSA mechanism, a scaling of the final ion energy with the laser power and pulse duration is given in [60]. Several experiments have been performed to understand the acceleration mechanism in micrometer thick foil targets [61, 62, 63, 64, 65, 66]. Although protons are preferentially accelerated due to their higher charge to mass ratio, it is found that heavier ions could be accelerated in a similar manner by suppressing the number of protons present in the impurity layer. This is done by removing the impurity proton layer by pre-heating the target [61]. Moreover, it is found that the removal of contaminants from the rear-side greatly reduce the proton number in the target, whereas their removal from the front side has no significant effect on the proton beam [67]. The use of thin targets ($\sim 1\mu m$) has resulted in a considerable increase in the maximum energy by restricting the electron movement in a confined space between the front and the rear target surface [55]. As a result, the hot electron population traverses several rounds inside the target thereby enhancing the number of hot electrons. This process of hot-electron recirculation assists the production of stronger electrostatic fields and hence increase the maximum energies of the ions. To optimise the generation of hot-electrons, a higher absorption of the laser energy to the electrons is essential. This can be ensured by using properly timed pre-pulses which can create pre-plasma at the target front. The optimum target thickness is found to be highly dependent on the pre-pulse duration [68]. The influence of the plasma scale-length was demonstrated in [69] where it is reported that the presence of a density gradient at the rear-side of the target degrades the proton beam energy.

The scaling of the maximum energy with the laser peak intensity for TNSA mechanism is given by $\varepsilon_{max} \propto a_0 \propto \sqrt{I_0}$. This makes the conversion efficiency for this scheme quite low. The exponential energy spectra makes the energy spread extremely broad ($\Delta\varepsilon/\varepsilon \approx 100\%$) which limits its

pertinence in certain applications requiring mono-energetic ions.

1.8.2 Radiation Pressure Acceleration

Another promising technique of accelerating ions is the Radiation Pressure Acceleration (RPA) and as the name suggests it utilises the strong light pressure of a high intensity laser. This mechanism of accelerating ions thus require extremely high laser intensities. The pressure exerted by an electromagnetic wave of intensity I on a plane surface at rest is given by

$$P_{rad} = (1 + R - T)\frac{I}{c} = (2R + A)\frac{I}{c} \tag{1.43}$$

where R, T, A are the reflection, transmission, and absorption coefficients respectively and therefore $R + T + A = 1$. These coefficients are functions of the refractive index of the medium and thus depend upon the wave frequency. Since the radiation pressure is directly related to the steady component of the ponderomotive force of the laser, its influence is stronger on the electrons than the ions ($f_P \propto \frac{1}{m}$, m is the particle mass). The displacement of the electrons due to the laser pressure results in the development of a charge separation field. This field further pulls the ions ahead of the laser pulse causing them to accelerate. For a laser of peak intensity $I_0 \sim 10^{20} W cm^{-2}$, laser pressure can exceed 100 Gbar which is well over the plasma thermal pressure of the solid-density target. The RPA is found to be dominant over the TNSA process with lasers of intensities exceeding $10^{23} W cm^{-2}$ [70]. Considering the presently available laser intensities, RPA generated protons are difficult to attain using linearly polarized lasers. However, it was observed that by using a circularly polarized laser, instead of a linear one, the intensity required for the onset of the radiation pressure action gets reduced to $I_0 \sim 10^{20} W cm^{-2}$ [71, 72]. Such laser intensities could easily be obtained at present. When a linearly polarized laser is incident normally on an opaque plasma target, the ponderomotive force becomes the cycled average of the $\vec{v} \times \vec{B}$ force, resulting in a strong absorption of the laser and subsequent hot electron generation. However for a steady drive of the electrons, it is essential for the plasma interface to act like a mirror

to the incident pulse. Therefore, radiation pressure action requires the plasma heating to be minimal. This condition could be taken care of by the use of a circularly polarized incident pulse. In case of a normally incident circularly polarized pulse, the oscillation component of the ponderomotive force vanishes. As a result the electrons remain at a locally balanced condition between the electrostatic force and the radiation pressure force. The comparatively low hot-electron temperatures using a circularly polarized laser result in a focused beam of ions and a narrow energy spectrum [73, 74].

The RPA mechanism causes a volumetric acceleration of the ions which

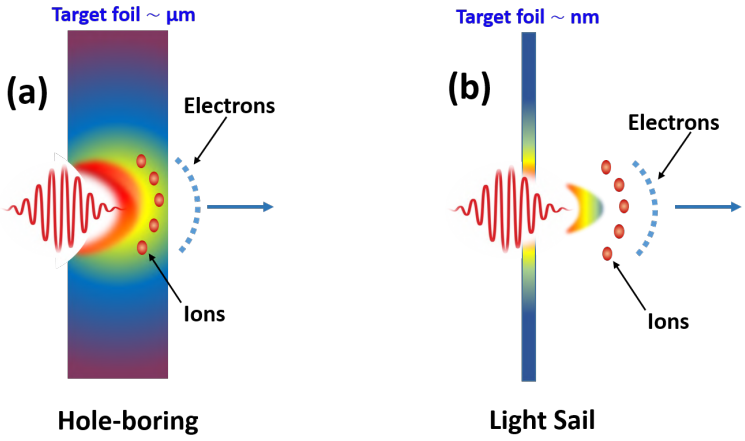

Figure 1.11: Representation of the RPA mechanism with an intense laser pulse ($I_0 > 10^{20} W cm^{-2}$ for a circularly polarized laser) irradiating a solid foil target. (a) Hole-boring: The plasma electrons from the thick ($\sim \mu m$) foil target are pushed by the laser pulse in a steady manner. The resultant charge separation field created due to the displaced electrons pulls the ions forward. (b) Light-sail: The electrons are completely expelled from the thin foil ($\sim nm$) by the action of the laser pressure. This results in the acceleration of the target as a whole.

is in contrast to the TNSA where ions are accelerated from the rear-surface. This property greatly reduces the energy spread of the RPA generated ion bunch. The scaling law with intensity $\varepsilon_{max} \sim I_0^m$ where $m \geq 1$ also suggests a favourable scaling compared to TNSA. Depending on the thickness of the foil target, radiation pressure acceleration may be categorized into two regimes. If the plasma target is thick ($\sim \mu m$), the RPA falls under the hole-boring (HB) regime. On the other hand, when the target is thin (of the order of the plasma skin-depth $\sim nm$),

the acceleration mechanism falls under the light-sail (LS) regime.

Hole-boring regime: Thick targets

The radiation pressure of the highly intense laser pulse pushes the plasma electrons inwards (into the target). The initially immobile ions experience a quasi-static charge separation field which is peaked at the separation layer between the displaced electrons and the lagged ions. This field pulls the ions towards the end of the electron layer causing the density to pile up in the region. The hole-boring process is shown in Fig.1.11 (a). The term "hole-boring" comes from the boring-effect caused by the laser pulse creating a parabolic density depression in the target front-surface. The velocity at which the density peak travels determines the final energies of the accelerated ions. The propagating density peak reflects ions present in the unperturbed plasma. These ions are then accelerated ahead of the hole-boring (high-density) layer. The quasi-constant velocity of the density spike, known as the hole-boring velocity v_{hb} is derived by equating the radiation pressure and reflected-ion pressure in the unperturbed region of the plasma in the hole-boring frame [75]. Considering the plasma surface to be perfectly reflecting,

$$2n_i m_i v_{hb}^2 = \frac{2I}{c} \tag{1.44}$$

Here, $m_i = Am_p$ and $n_i = Zn_e$ are the mass and density of the reflected ions and I is the intensity of the electromagnetic wave. Therefore,

$$\frac{v_{hb}}{c} = \sqrt{\frac{I}{n_i m_i c^3}} = \sqrt{\Pi} \tag{1.45}$$

Here, $\Pi = \dfrac{I}{n_i m_i c^3} = \dfrac{m_e n_c}{m_i n_i} a_0^2 = \dfrac{Z m_e n_c}{A m_p n_e} a_0^2$. The velocity of the reflected ions in the lab-frame thus becomes $v_i = 2v_{hb} = 2\sqrt{\dfrac{I}{n_i m_i c}}$. Correspondingly, the ion energy (ε_i) for this non-relativistic case in the lab-frame is given by $\varepsilon_i = 2m_i c^2 \Pi$. Implementing relativistic corrections to the theory, the expressions for the hole-boring velocity and the ion energy have been

modified as [76, 77],

$$\frac{v_{hb}}{c} = \frac{\sqrt{\Pi}}{1+\sqrt{\Pi}} \tag{1.46}$$

$$\varepsilon_i = 2m_i c^2 \frac{\Pi}{1+2\sqrt{\Pi}} \tag{1.47}$$

The scaling of the ion energy with the laser intensity suggests a preferential scaling in the non-relativistic case where $\varepsilon_i \propto I$ compared to the relativistic case where $\varepsilon_i \propto \sqrt{I}$.

The hole-boring action of the laser can take place only if the plasma target is overdense. Considering the high intensity of the laser, the critical layer for the laser propagation gets modified to γn_c (relativistic transparency) where γ is the electron Lorentz relativistic factor. However, it was found that the laser propagation stops even with $n_e < \gamma n_c$. The compression layer at the target front-surface creates a high-density region which allows hole-boring mechanism to take place even with an originally less dense target [78]. This suggests protons of energy around $200MeV$ could be achieved using hole-boring acceleration of ions using a laser of intensity $I_0 \sim 10^{21} W cm^{-2}$ [79].

Light-sail regime: Thin targets

The light sail regime acts on the ions in a much thinner (usually of the order of the skin-depth, δ_s) foil compared to the hole-boring case. In this situation the target is thin enough so that all the ions inside the target are accelerated before the edge of the laser pulse reaches the rear-surface of the target. The boost from the laser's radiation pressure on the target, having a large surface area, low thickness and, low mass makes it act like a "light-sail" that sweeps though vacuum ahead of the laser pulse. The compressed electron and ion double-layer gets completely detached from the foil target and gets accelerated as a separate plasma entity [70]. As these segregated ions are no longer shielded by the background plasma ions, they can get accelerated to very high energies. This regime is manifested in case of lasers having ultra-high contrast ratios and ultra-short pulse duration. This is to ensure that the foil remains

intact for the peak of the laser. The light-sail mechanism is schematically represented in Fig. 1.11 (b). In the non-relativistic limit, the acceleration of the ions from a foil target of density $\rho = m_i n_i$ and thickness d is given by,

$$\frac{dv_{ls}}{dt} = \frac{(1+R)}{\rho dc} I = \frac{(1+R)}{m_i n_i dc} I \tag{1.48}$$

Therefore, in the light-sail regime, the velocity of the ions scale linearly with the laser intensity, which would imply that their energy follows a scaling law $\varepsilon_i \propto I^2$. In the relativistic case, the Doppler down-shift needs to be taken into account which would modify this expression of acceleration [80]. It can be inferred therefore, that, for an ultra-thin target of very low density, the energy yield will be very high. However, it should be noted that for the radiation pressure of the laser to act upon the target, it must be overdense. Moreover, in case of an extremely thin target, the interaction with the intense laser runs the risk of knocking out the electrons completely from the target. This may cause the electrons to dissociate from the ions, thus breaking the balance between the radiation pressure force and the electrostatic force. Therefore, there must exist a limiting thickness d_m beyond which all the electrons escape from the interaction leaving behind a positively charged target core. Assuming there is no transverse heating due to the spatial spread of the laser, the minimum thickness of the foil for the light-sail action to play while getting impinged by a circularly polarized laser of strength parameter a_0 is given by

$$\frac{d_m}{\lambda} = \frac{a_0}{\pi} \sqrt{\frac{(1+R)}{2}} \frac{n_c}{n_e} \tag{1.49}$$

This limiting thickness is evaluated considering a one-dimensional model which unrealistically simplifies the scenario. In the multi-dimensional geometry, the expansion of the plasma in the transverse dimension will lead to an early onset of transparency in the target and therefore inhibit the effect of the light-sail mechanism.

1.8.3 Collisionless Shock Acceleration

The density steepening caused due to the ponderomotive action of the laser at the surface of the target may give rise to electrostatic shocks. Theoretically, a shock is generated by the propagation of a physical perturbation with a velocity greater than the sound velocity in that particular medium [81]. Thus for a shock propagating with velocity v_s, the Mach number $M = \frac{v_s}{c_s} > 1$. Here, $c_s = \sqrt{\frac{Zk_BT_e}{Am_p}}$ is the ion-acoustic velocity in the medium. A sudden jump in the plasma density that originates at the interaction layer and propagate through the plasma bulk might lead to the generation of an electrostatic shock wave. These shocks are collisionless as they are supported by charge-separation fields, which make them different from hydrodynamic shocks which are sustained by collisions and viscous drag effects. The ions that are in the unperturbed region of the plasma (upstream of the shock) might get reflected elastically from the shock front and acquire velocities upto twice the shock velocity ($v_i = 2v_s$) in the laboratory frame of reference. The condition for reflection of the upstream ions from the shock front having an electrostatic potential barrier height ϕ_{es} is $Ze\phi_{es} > \frac{mv_i^2}{2}$; v_i being the ion velocity in the shock frame. The ions after getting reflected from the shock acquire energy (per nucleon) $\varepsilon_{CSA} = 2m_pv_s^2$, considering the shock velocity v_s to be non-relativistic. The shock accelerated ions are found to have a very narrow energy bandwidth in the ion spectra, showing strong potential for application purposes. Haberberger et al. [82] were able to generate highly mono-energetic ($\sim 1\%$ energy spread) protons with energy $22MeV$ using CO_2 lasers and a hydrogen gas jet as the target. They also suggested that using a CO_2 laser of intensity $\sim 10^{18}Wcm^{-2}$ has the capacity to produce protons with energy exceeding $200MeV$.

Collisionless shock acceleration (CSA) as a mechanism to accelerate ions from an overdense plasma target using highly intense lasers was reported by Denavit [75] using 1D simulations and showed that the target heating by the laser pulse governs the shock formation. Later it was found by Silva et al. [83] that using thin targets can cause refluxing of the

electrons leading to enhanced electron temperatures. This facilitates the generation of a fast shock ($M = 2-3; v_s > 0.1c$) which can reflect ions to very high energies. The shock accelerated ions might get a further boost due to the rear-side TNSA field while travelling through the plasma. This accounts for a staged CSA-TNSA process that contribute to the highest energetic ions in the energy spectrum [84, 85]. The maximum energy of the ions depend on both the mechansims with the fastest ions travelling with velocity $v_i = 2v_s + v_{sheath}$, with v_{sheath} being the contribution from the rear-surface sheath field [86]. The ions are dominantly accelerated by CSA if the velocities attained from the shock front is higher than the velocity provided by the sheath field, i.e. $2v_s > V_{sheath}$. A thinner target facilitates the CSA mechanism preferentially over TNSA. The resultant ion velocity provided by this mechanism causes a broader energy spread and is characterized by a plateau in the ion spectra [83]. Since CSA could be achieved using a overdense target which also supports the generation of hole-boring conditions, it is essential to state that the shock travels faster than the hole-boring density layer, i.e. $v_{sh} > v_{hb}$. This makes CSA capable of providing higher energies to ions, as compared to RPA. However, to maintain a narrow energy spread of the ions, it is necessary that the number of ions accelerated from the shock remains low. A large number of shock reflected ions will cause the shock to lose energy in the long run (because of momentum transfer) and at later stages of the acceleration process, the ions will be reflected with lesser energy causing the energy spectrum to broaden [87]. Detailed descriptions of the shock acceleration mechanisms are dedicated in the upcoming chapters of this thesis for specific scenarios.

1.8.4 Breakout Afterburner: Relativistically transparent targets

The Breakout Afterburner (BOA) or the Relativistically Induced Transparency (RIT) ion acceleration scheme comes into action when the target density drops from being over-dense to a relativistically transparent ($n_e = \gamma n_c$) regime after getting impinged with a superintense laser pulse.

This mechanism was first reported by Yin et al. [88, 89] and the relativistic modification to the theoretical model was made by Albright et al.[90]. The interaction of an intense linearly polarized laser pulse with a thin foil target, under appropriate conditions, can have three phases of acceleration. Initially as the foil is opaque to the laser pulse, the absorption of the laser at the skin depth layer transfers the energy to the electrons which generates the electrostatic sheath field at the rear surface, required for the TNSA process. Now as the foil is sufficiently thin, a very large number of electrons are thermally agitated leading to plasma expansion. This brings forth the second phase of the acceleration process: the enhanced TNSA phase. As a consequence of plasma expansion the plasma density drops from its initially overdense value so that the plasma skin depth is of the order of the target thickness. Once the density drops below γn_c (relativistically critical density), the laser pulse can propagate inside the expanded hot plasma, causing the onset of breakout afterburner. Contrary to TNSA being a surface phenomena, BOA takes into account all the electrons present inside the plasma making it a volumetric phenomena. With the ions already flowing along the laser propagation direction due to the TNSA processes (both normal and enhanced TNSA), they are now joined by the hot electrons (caused by the BOA process) accelerating in the same direction from the target bulk. The thermal electrons move with relativistic velocities that are much higher than the ion velocities (non-relativistic). The difference in the velocities of the flowing ions and the electrons result in a two-stream instability, known as the Buneman instability [91]. The instability resonates with the ions, and in an effort to reduce the relative drift velocity, supplies energy to the ions from the electrons. The electrons losing energy to the ions are again reheated from the propagating laser pulse and the process can continue for a long time till the laser field dies out. The ions draw out a broad energy distribution in the spectra with very high cutoff energies. A stronger coupling of the laser energy into electrons and the eventual translation to fast ions make the BOA/RTI acceleration scheme a promising phenomena for an efficient ion source.

1.8.5 Coulomb Explosion

When the target size is sufficiently small or the laser intensity is very high, the laser ponderomotive effect can blow off the entire electron population from the target bulk. The unbalanced positive ions remaining in the bulk region will thus explode isotropically due the strong Coulombic repulsion among the ions. The explosion provides high kinetic energy to the ions, with the fastest ions acquiring tens of $MeVs$ of energies [92]. The characteristic energy spectra of the ions accelerated through Coulomb explosion is such that the number of ions per unit energy $\frac{dN}{d\varepsilon}$ increases as $\sqrt{\varepsilon}$ [93] before reaching a cutoff energy given by

$$\varepsilon_C = \frac{4\pi}{3} Z^2 e^2 n_i R_t^2 \tag{1.50}$$

Here R_t is the radius of the spherical ion cloud of density n_i. An anisotropy can be introduced to the Coulomb exploded ions by conditioning the laser pressure to push the plasma ions preferentially in the longitudinal direction. This provides a directionality to the ions and reduces their energy spread in the ion spectra [94].

1.9 Advanced target geometries

Typically, most of the initial experiments dedicated to the generation of energetic ions by accelerating them with the help of an intense laser use extended flat foils of solid density (having transverse dimensions much greater than the laser focal area). However, it was found that by using a target with transverse dimension comparable to the laser focal spot, the laser energy coupling to the electrons increases significantly. The increase in the laser absorption is eventually translated to an enhancement in the maximum energies of the ions [95]. This is because of the reduced lateral expansion of the hot electrons from the interaction site which leads to a confinement of the laser energy onto a localised region, generating a powerful accelerating field [96, 97, 98]. Therefore, in the last decade or so, the ion acceleration studies using intense laser pulses have shifted at-

tention on to such targets of reduced dimensions, termed as mass-limited targets (MLTs).

The geometry of the target has an important role to play in the generation of energetic ion bunches. Several simulation and experimental works have suggested spherical targets for the generation of fast ions [99, 100, 101, 102, 103]. If the target diameter is of the order of the laser spot size, the loss in laser energy is minimal and the fast electron generation also helps in increasing the ion energy [95]. The curved front surface of the target helps in converging the ions into a narrow region and quasi-monoenergetic structures can be observed in the ion spectra [100, 104]. A focused ion beam is essential for several applications, and therefore studies on diverse target geometries have been made to enhance the collimation of the fast ions along with their maximum energies. Concave parabolic shaped targets [105] are reported to enhance the accelerating electric fields, and laser intensities required for optimum action of RPA mechanism is found to get suppressed by more than an order of magnitude using dual parabolic targets [106]. On the other hand, convex targets help in maintaining a uniform acceleration through RPA for a longer duration of time compared to conventional flat targets [107]. Such bulged targets also helps in guiding the accelerated proton bunch along the laser axis[108]. Modified conical targets have also been used for their strong electron heating and efficient ion guiding system [109, 110]. Protons of maximum cutoff energy 67.5 MeV was obtained from the experimental study using a flat-top hollow microcone target as reported by Gaillard et al. [111]. The curved walls of the cone focuses the laser pulse as it moves through the expanded plasma before interacting with the flat-top region. A resultant enhancement in the number of hot electrons aids in increasing the maximum proton energy.

1.10 Methodology: Particle-In-Cell (PIC) simulation

The complex nature of plasma and its intricate properties and conditions makes it usually difficult for non-linear analytical treatment. This has inspired a branch of plasma physics termed as plasma simulation, which complements the growth in experimental studies of plasma environments. Laser-plasma experiments, specifically, can sometimes be too expensive, or might require very high laser intensities which are presently unavailable. In such scenarios, simulation studies might be extremely helpful for comprehension of the real system in a virtual experiment. Moreover, computer simulations can also be used for the designing and prediction of future experiments.

The Particle-In-Cell simulation method is a popular and effective way to solve many-body systems interacting with long-range forces (eg. plasmas). The PIC simulation codes are used to completely simulate the dynamics of the electrons and ions of the plasma in presence of electromagnetic fields (the laser). The fundamental aspect of PIC simulation is to divide the computational space into distinct cells, and the intersecting points of the cells are known as the mesh points or grid points. The discretization has to be done by considering the stability condition, $\Delta t < \frac{\Delta x}{c\sqrt{d}}$, known as the Courant stability condition; where, Δt is the time step, Δx is the smallest cell size, c is the velocity of light and $d = 1, 2, 3$ corresponding to 1, 2 and 3-dimensional problems respectively. The plasma particles (both electrons and ions) are grouped together in sets, known as the macroparticle (or the super-particle). Each macroparticle represents a number of real plasma particles and have the same charge to mass ratio as the original particle that it represents. The Lorentz force equation is solved for each macroparticle, instead of each real particle, reducing the computational load.

The PIC-cycle

One complete cycle of the simulation scheme can be represented as Fig. 1.12. The following points sum up the process:

- The particle positions (x_i) and velocities (v_i) are discretized to charge and current densities (ρ and J respectively) that are calculated at the grid points by an interpolation method called the weighting.
- The calculated charge densities and the current densities now becomes the source terms in the Maxwell's field equations. The electric and the magnetic fields are thus computed at the grid points.
- The electric and magnetic fields are then utilized to solve the discretized Lorentz equation to calculate the force on the macroparticle.
- The force is then integrated to determine the updated set of velocities and positions for the new time-cycle. The entire cycle is then repeated for the entire time of simulation (till the maximum time-step is reached) for each individual macroparticle.

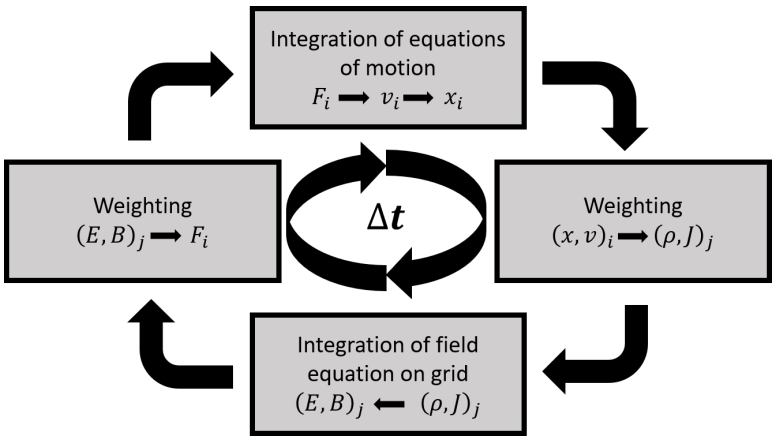

Figure 1.12: A typical time-cycle of the PIC simulation of a single macroparticle [112]

Solving the field equations

The advancement of the electric ($\vec{E}$) and magnetic ($\vec{B}$) fields are made by solving the Maxwell's equations which are discretized in space. In

a three-dimensional geometry, the three components of the field vectors along the three perpendicular directions are computed on the grid points. The Yee cell [113] represents the alignment of these field quantities [Fig. 1.13]. The Finite-difference Time-domain (FDTD) method is utilised to solve the Maxwell's equations that are discretized in space and time as a center-difference form and the electric and magnetic fields are separated in time by half a time increment. With the time increment in each PIC cycle given by Δt, the electric field is calculated at integral values of Δt as $(..., (n-1), n, (n+1), ...)$ whereas the magnetic fields and the current densities are determined at half-integral values of Δt as $(..., (n-\frac{1}{2}), (n+\frac{1}{2}), (n+\frac{3}{2}), ...)$. The grid size along the three directions Δx, Δy, Δz are used as the units to define the positions.

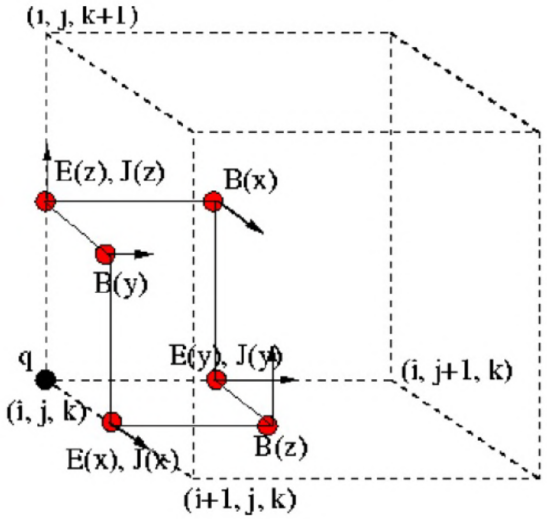

Figure 1.13: A typical Yee cell. The components of E, B and J are attached to the cell with vertex (i,j,k). These components are displaced by half times the cell dimension. The J and E components are calculated at the edges of the cell, while the B components are associated with the face of the cell. The charge q is calculated at the grid points. [113]

The x-component of the magnetic field at the grid point (i,j,k) is advanced from time step $(n-1/2)$ to $(n+1/2)$, and for that, the values of E_y and E_z and J_x of the surrounding grid points at time-step n are required. Using the Yee cell, x-component of the curl of the electric field

at a grid point (i,j,k) is expressed as,

$$\frac{E^n_{z(i,j+1,k)} - E^n_{z(i,j,k)}}{\Delta y} - \frac{E^n_{y(i,j,k+1)} - E^n_{y(i,j,k)}}{\Delta z} = -\frac{1}{c}\frac{B^{n+1/2}_{x(i,j,k)} - B^{n-1/2}_{x(i,j,k)}}{\Delta t} \tag{1.51}$$

In a similar manner, for the advancement of the x-component of the electric field at grid point (i,j,k) from time step n to $(n+1)$, the values of B_y, B_z and J_x of the neighbouring grid points at time-step $(n+1/2)$ are utilized. The x-component of the curl of the magnetic field at a grid point (i,j,k) is expressed as,

$$\frac{B^{n+1/2}_{z(i,j,k)} - B^{n+1/2}_{z(i,j-1,k)}}{\Delta y} - \frac{B^{n+1/2}_{y(i,j,k)} - B^{n+1/2}_{y(i,j,k-1)}}{\Delta z} = \frac{4\pi}{c} J^{n+1/2}_{x(i,j,k)} + \frac{E^{n+1}_{x(i,j,k)} - E^n_{x(i,j,k)}}{c\Delta t} \tag{1.52}$$

The momentum advance

The momentum advancement is made using the Lorentz force equation which can be expressed in the central-difference form as

$$\vec{p}^{n+1/2} - \vec{p}^{n-1/2} = q\left[\vec{E}^n \Delta t + \frac{1}{c}\left\{\vec{v}^n \times \vec{B}^n\right\}\right] \tag{1.53}$$

Here, the momentum and fields are separated by half a time-step. The E^n and B^n calculated at the grid points are now computed at the macroparticle positions by means of a trilinear interpolation that is carried out relativistically using the Boris method [112].

The position advance

For each macroparticle, its position is now advanced using $\frac{\partial \vec{r}}{\partial t} = \vec{v}$ which can be written in a central-difference form as

$$\vec{r}^{n+1} - \vec{r}^n = \vec{v}^{n+1/2}\Delta t \tag{1.54}$$

The process is done using the leap-frog mechanism shown in Fig. 1.14

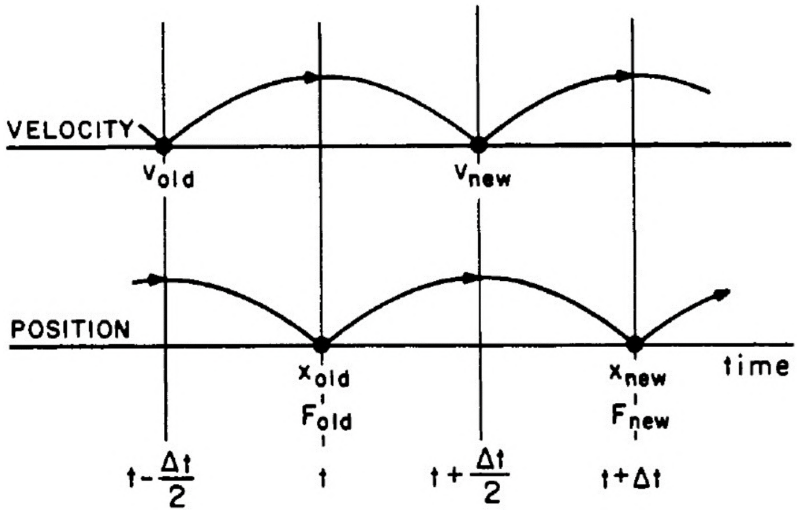

Figure 1.14: The leap-frog integration scheme which uses time-centering of the force ($\vec{F}$) to advance the velocity ($\vec{F}$) and then time-centering of t($\vec{v}$) is done to advance the position ($\vec{r}$) [112].

Particle weighting

An interpolation method called Weighting is used to evaluate the charge densities at the grid points from the known positions and velocities of the particles nearest to the grid point, at the given time-step. Under this method, an assumption is made that the charged particles are rigid clouds of finite size that move freely through the cells [see Fig. 1.15]. Considering a single dimension, the particle of charge q_c and size Δx is assumed to be of uniform density. Therefore, the amount of charge assigned to a grid point j for a particle positioned at x_i is

$$q_j = q_c \left[\frac{\Delta x - (x_i - X_j)}{\Delta x} \right] = q_c \left[\frac{X_{j+1} - x_i}{\Delta x} \right] \tag{1.55}$$

and to grid (j+1) is

$$q_{j+1} = q_c \left[\frac{x_i - X_j}{\Delta x} \right] \tag{1.56}$$

The particles' position at time n and $n+1$ and the velocities at time $(n+\frac{1}{2})$ are then used to interpolate the current densities at the grids averaged over the time-steps. For a particle at position x_i having velocity

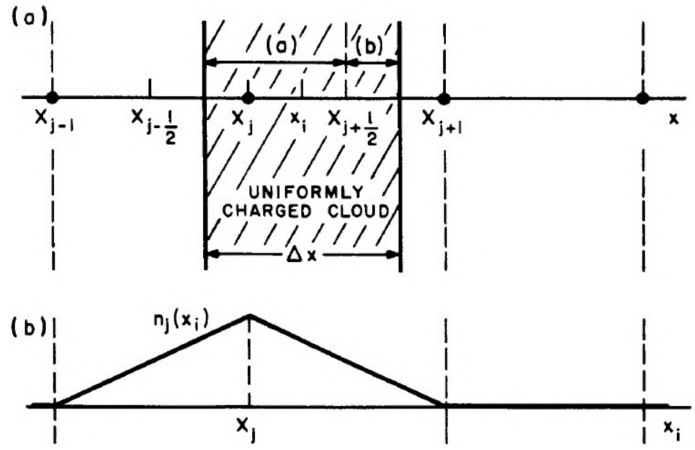

Figure 1.15: First order weighting process to calculate the charge densities: (a) The fraction of the charge cloud inside the j^{th} cell is interpolated as X_j [fraction (a)] and the fraction of the charge cloud inside the $(j+1)^{th}$ cell is interpolated as X_{j+1} [fraction (b)]]. (b) The grid density $n_j(x_i)$ at x_i as the particle move past X_j displaying the effective particle shape $S(x)$ [112].

$\vec{v}_i^{n+1/2}$, the current density $\vec{J}^{n+1/2}$ at grid j is written as

$$\vec{J}_j^{n+1/2} = \sum_i q_i \vec{v}_i^{n+1/2} \frac{1}{2} \left[S(X_j - x_i^{n+1}) + S(X_j - x_i^n) \right] \tag{1.57}$$

Here, $S(x)$ is a spatial interpolation function.

The weighting of fields and force are done in a similar manner. In the linear interpolation method, for a particle at x_i, the electric field $\vec{E}$ is interpolated as

$$\vec{E}(x_i) = \left[\frac{X_{j+1} - x_i}{\Delta x} \right] \vec{E}_j + \left[\frac{x_i - X_j}{\Delta x} \right] \vec{E}_{j+1} \tag{1.58}$$

Higher-order weighting schemes further smoothens the particle shape and reduces noises in the evaluation of density and fields. This comes at the cost of higher computation power.

In the PIC scheme, the distribution functions of the particles are statistically represented in phase space. Relativistic effects are often incorporated in the treatment of the particles with very less approximations. This helps in holding the physics true a great deal of time. Despite several advantages, there also exists some disadvantages of PIC mechanism. The numerical heating in the system decays as $\frac{1}{\sqrt{N}}$ for N number of

macroparticles. So, for a smooth, noise-free distribution, the number of particles should ideally be very large. Moreover, due to the constraints on Δt and cell size, simulating high N particles with high density for a long time-scale in a large simulation domain requires extremely powerful computation resources and are very costly. However, this cost can be optimized by cleverly choosing the real and simulation parameters without losing much of the actual physics.

1.11 Thesis structure

In this thesis, efficient acceleration of protons from a spherical micrometre-sized plasma target is studied after interaction with an ultrashort intense laser pulse. The spherical shape of the target assists the formation of an energetic proton bunch which is a result of synergy between various acceleration processes. Different target density distributions are introduced and their influence on the subsequent proton dynamics is analysed.

The present thesis has been laid out in the subsequent chapters as follows:

In **Chapter 2**, a spherical plasma of uniform density having dimensions comparable to the laser focal spot has been analysed after interaction with a short intense laser pulse. The 3D PIC simulation is dedicated to identify the acceleration processes of the plasma ions.

In **Chapter 3**, the plasma sphere is considered to be pre-exploded due to interaction with a laser pre-pulse. The modification in the density profile due to the target pre-expansion is analysed and the consequent ion dynamics is studied after interaction with the high-intensity main pulse.

In **Chapter 4**, a Gaussian variation is considered in the density distribution of the plasma sphere. The low peak density at the centre results in a fast expansion of the target after interacting with the laser pulse. The expansion mechanism is studied in this chapter keeping the focus on fast proton generation.

In **Chapter 5**, the study on the Gaussian shaped density distribution is

extended for steeper gradients. A comparison is also made with a flat foil target and the energetic proton yield is found to be higher for the sphere targets.
Finally, in **Chapter 6**, a summary of the work included in this thesis is provided with a brief discussion on the future prospects related to this study

Bibliography

[1] Maiman, T. H. Stimulated optical radiation in ruby. *Nature*, 187:494, 1960.

[2] Strickland, D. and Mourou, G. Compression of amplified chirped optical pulses. *Optics communications*, 55(6):447–449, 1985.

[3] Hatchett, S. P., Brown, C. G., Cowan, T. E., Henry, E. A., Johnson, J. S., Key, M. H., Koch, J. A., Langdon, A. B., Lasinski, B. F., Lee, R. W., et al. Electron, photon, and ion beams from the relativistic interaction of petawatt laser pulses with solid targets. *Phys. Plasmas*, 7(5):2076–2082, 2000.

[4] Modena, A., Najmudin, Z., Dangor, A., Clayton, C., Marsh, K., Joshi, C., Malka, V., Darrow, C., Danson, C., Neely, D., et al. Electron acceleration from the breaking of relativistic plasma waves. *Nature*, 377(6550):606–608, 1995.

[5] Esarey, E., Sprangle, P., Krall, J., and Ting, A. Overview of plasma-based accelerator concepts. *IEEE Transactions on plasma science*, 24(2):252–288, 1996.

[6] Malka, V., Fritzler, S., Lefebvre, E., Aleonard, M.-M., Burgy, F., Chambaret, J.-P., Chemin, J.-F., Krushelnick, K., Malka, G., Mangles, S., et al. Electron acceleration by a wake field forced by an intense ultrashort laser pulse. *Science*, 298(5598):1596–1600, 2002.

[7] Mangles, S. P., Murphy, C., Najmudin, Z., Thomas, A. G. R., Collier, J., Dangor, A. E., Divall, E., Foster, P., Gallacher, J.,

Hooker, C., et al. Monoenergetic beams of relativistic electrons from intense laser–plasma interactions. *Nature*, 431(7008):535–538, 2004.

[8] Leemans, W. P., Nagler, B., Gonsalves, A. J., Tóth, C., Nakamura, K., Geddes, C. G., Esarey, E., Schroeder, C., and Hooker, S. Gev electron beams from a centimetre-scale accelerator. *Nature physics*, 2(10):696–699, 2006.

[9] Schlenvoigt, H.-P., Haupt, K., Debus, A., Budde, F., Jäckel, O., Pfotenhauer, S., Schwoerer, H., Rohwer, E., Gallacher, J., Brunetti, E., et al. A compact synchrotron radiation source driven by a laser-plasma wakefield accelerator. *Nature Physics*, 4(2):130–133, 2008.

[10] Grüner, F., Becker, S., Schramm, U., Eichner, T., Fuchs, M., Weingartner, R., Habs, D., Meyer-ter Vehn, J., Geissler, M., Ferrario, M., et al. Design considerations for table-top, laser-based vuv and x-ray free electron lasers. *Applied Physics B*, 86(3):431–435, 2007.

[11] Wang, W., Feng, K., Ke, L., Yu, C., Xu, Y., Qi, R., Chen, Y., Qin, Z., Zhang, Z., Fang, M., et al. Free-electron lasing at 27 nanometres based on a laser wakefield accelerator. *Nature*, 595(7868):516–520, 2021.

[12] Tripathi, V. and Liu, C. Self-generated magnetic field in an amplitude modulated laser filament in a plasma. *Phys. Plasmas*, 1(4):990–992, 1994.

[13] Sentoku, Y., Ruhl, H., Mima, K., Kodama, R., Tanaka, K., and Kishimoto, Y. Plasma jet formation and magnetic-field generation in the intense laser plasma under oblique incidence. *Phys. Plasmas*, 6(7):2855–2861, 1999.

[14] Sprangle, P., Esarey, E., and Ting, A. Nonlinear theory of intense laser-plasma interactions. *Phys. Rev. Lett*, 64(17):2011, 1990.

[15] Esarey, E., Ting, A., Sprangle, P., Umstadter, D., and Liu, X. Nonlinear analysis of relativistic harmonic generation by intense lasers in plasmas. *IEEE transactions on plasma science*, 21(1):95–104, 1993.

[16] Gibbon, P. High-order harmonic generation in plasmas. *IEEE Journal of Quantum Electronics*, 33(11):1915–1924, 1997.

[17] Bulanov, S., Esirkepov, T. Z., Naumova, N., Pegoraro, F., and Vshivkov, V. Solitonlike electromagnetic waves behind a superintense laser pulse in a plasma. *Phys. Rev. Lett*, 82(17):3440, 1999.

[18] Borghesi, M., Bulanov, S., Campbell, D., Clarke, R., Esirkepov, T. Z., Galimberti, M., Gizzi, L., MacKinnon, A., Naumova, N., Pegoraro, F., et al. Macroscopic evidence of soliton formation in multiterawatt laser-plasma interaction. *Phys. Rev. Lett*, 88(13):135002, 2002.

[19] Veksler, V. The principle of coherent acceleration of charged particles. *The Soviet Journal of Atomic Energy*, 2(5):525–528, 1957.

[20] Tajima, T. and Dawson, J. M. Laser electron accelerator. *Phys. Rev. Lett*, 43(4):267, 1979.

[21] Clark, E., Krushelnick, K., Davies, J., Zepf, M., Tatarakis, M., Beg, F., Machacek, A., Norreys, P., Santala, M., Watts, I., et al. Measurements of energetic proton transport through magnetized plasma from intense laser interactions with solids. *Phys. Rev. Lett*, 84(4):670, 2000.

[22] Maksimchuk, A., Gu, S., Flippo, K., Umstadter, D., and Bychenkov, V. Y. Forward ion acceleration in thin films driven by a high-intensity laser. *Phys. Rev. Lett*, 84(18):4108, 2000.

[23] Snavely, R., Key, M., Hatchett, S., Cowan, T., Roth, M., Phillips, T., Stoyer, M., Henry, E., Sangster, T., Singh, M., et al. Intense high-energy proton beams from petawatt-laser irradiation of solids. *Phys. Rev. Lett.*, 85(14):2945, 2000.

[24] Wilks, S., Langdon, A., Cowan, T., Roth, M., Singh, M., Hatchett, S., Key, M., Pennington, D., MacKinnon, A., and Snavely, R. Energetic proton generation in ultra-intense laser–solid interactions. *Phys. Plasmas*, 8(2):542–549, 2001.

[25] Wilson, R. R. Radiological use of fast protons. *Radiology*, 47(5):487–491, 1946.

[26] Giap, H., Roda, D., and Giap, F. Can proton beam therapy be clinically relevant for the management of lung cancer? *Radiation and Combined Therapies for Lung Cancer*, 78, 2015.

[27] What is proton therapy? `http://w3.ai-hosp.or.jp/_en/ptc/what_ptc.html`, 2016. Accessed: 2022-02-10.

[28] Bulanov, S. and Khoroshkov, V. Feasibility of using laser ion accelerators in proton therapy. *Plasma Physics Reports*, 28(5):453–456, 2002.

[29] Bulanov, S., Esirkepov, T. Z., Khoroshkov, V., Kuznetsov, A., and Pegoraro, F. Oncological hadrontherapy with laser ion accelerators. *Physics Letters A*, 299(2-3):240–247, 2002.

[30] Bulanov, S. V., Wilkens, J. J., Esirkepov, T. Z., Korn, G., Kraft, G., Kraft, S. D., Molls, M., and Khoroshkov, V. S. Laser ion acceleration for hadron therapy. *Physics-Uspekhi*, 57(12):1149, 2014.

[31] Malka, V., Fritzler, S., Lefebvre, E., d'Humières, E., Ferrand, R., Grillon, G., Albaret, C., Meyroneinc, S., Chambaret, J.-P., Antonetti, A., et al. Practicability of protontherapy using compact laser systems. *Medical physics*, 31(6):1587–1592, 2004.

[32] Koehler, A. Proton radiography. *Science*, 160(3825):303–304, 1968.

[33] Borghesi, M., Campbell, D., Schiavi, A., Haines, M., Willi, O., MacKinnon, A., Patel, P., Gizzi, L., Galimberti, M., Clarke, R., et al. Electric field detection in laser-plasma interaction experiments via the proton imaging technique. *Phys. Plasmas*, 9(5):2214–2220, 2002.

[34] Borghesi, M., Romagnani, L., Schiavi, A., Campbell, D., Haines, M., Willi, O., Mackinnon, A., Galimberti, M., Gizzi, L., Clarke,

R., et al. Measurement of highly transient electrical charging following high-intensity laser–solid interaction. *Applied Physics Letters*, 82(10):1529–1531, 2003.

[35] Mackinnon, A., Patel, P., Town, R., Edwards, M., Phillips, T., Lerner, S., Price, D., Hicks, D., Key, M., Hatchett, S., et al. Proton radiography as an electromagnetic field and density perturbation diagnostic. *Review of Scientific Instruments*, 75(10):3531–3536, 2004.

[36] Cecchetti, C., Borghesi, M., Fuchs, J., Schurtz, G., Kar, S., Macchi, A., Romagnani, L., Wilson, P., Antici, P., Jung, R., et al. Magnetic field measurements in laser-produced plasmas via proton deflectometry. *Phys. Plasmas*, 16(4):043102, 2009.

[37] Romagnani, L., Fuchs, J., Borghesi, M., Antici, P., Audebert, P., Ceccherini, F., Cowan, T., Grismayer, T., Kar, S., Macchi, A., et al. Dynamics of electric fields driving the laser acceleration of multi-mev protons. *Phys. Rev. Lett*, 95(19):195001, 2005.

[38] Faenov, A. Y., Pikuz, T. A., Fukuda, Y., Kando, M., Kotaki, H., Homma, T., Kawase, K., Kameshima, T., Pirozhkov, A., Yogo, A., et al. Ionography of nanostructures with the use of a laser plasma of cluster targets. *JETP letters*, 89(10):485–491, 2009.

[39] Patel, P., Mackinnon, A., Key, M., Cowan, T., Foord, M., Allen, M., Price, D., Ruhl, H., Springer, P., and Stephens, R. Isochoric heating of solid-density matter with an ultrafast proton beam. *Phys. Rev. Lett*, 91(12):125004, 2003.

[40] Tabak, M., Hammer, J., Glinsky, M. E., Kruer, W. L., Wilks, S. C., Woodworth, J., Campbell, E. M., Perry, M. D., and Mason, R. J. Ignition and high gain with ultrapowerful lasers. *Phys. Plasmas*, 1(5):1626–1634, 1994.

[41] Bychenkov, V. Y., Rozmus, W., Maksimchuk, A., Umstadter, D., and Capjack, C. Fast ignitor concept with light ions. *Plasma Physics Reports*, 27(12):1017–1020, 2001.

[42] Honrubia, J., Fernández, J., Temporal, M., Hegelich, B., and Meyer-ter Vehn, J. Fast ignition of inertial fusion targets by laser-driven carbon beams. *Phys. Plasmas*, 16(10):102701, 2009.

[43] Roth, M., Cowan, T., Key, M., Hatchett, S., Brown, C., Fountain, W., Johnson, J., Pennington, D., Snavely, R., Wilks, S., et al. Fast ignition by intense laser-accelerated proton beams. *Phys. Rev. Lett.*, 86(3):436, 2001.

[44] Atzeni, S., Temporal, M., and Honrubia, J. A first analysis of fast ignition of precompressed icf fuel by laser-accelerated protons. *Nuclear fusion*, 42(3):L1, 2002.

[45] Temporal, M., Honrubia, J., and Atzeni, S. Numerical study of fast ignition of ablatively imploded deuterium–tritium fusion capsules by ultra-intense proton beams. *Phys. Plasmas*, 9(7):3098–3107, 2002.

[46] Fernández, J. C., Albright, B. J., Flippo, K. A., Hegelich, B. M., Kwan, T. J., Schmitt, M. J., and Yin, L. Progress on ion based fast ignition. In *Journal of Physics: Conference Series*, volume 112, 022051. IOP Publishing, 2008.

[47] Hegelich, B., Jung, D., Albright, B., Fernandez, J., Gautier, D., Huang, C., Kwan, T., Letzring, S., Palaniyappan, S., Shah, R., et al. Experimental demonstration of particle energy, conversion efficiency and spectral shape required for ion-based fast ignition. *Nuclear Fusion*, 51(8):083011, 2011.

[48] Chen, F. Introduction to plasma physics and controlled fusion. *Plenum Press, New York*, 1984.

[49] Kruer, W. *The physics of laser plasma interactions*. CRC Press, 2019.

[50] Macchi, A. *A Superintense Laser-Plasma Interaction Theory Primer*. Springer Science & Business Media, 2013.

[51] Daido, H., Nishiuchi, M., and Pirozhkov, A. S. Review of laser-driven ion sources and their applications. *Reports on progress in physics*, 75(5):056401, 2012.

[52] Brunel, F. Not-so-resonant, resonant absorption. *Phys. Rev. Lett*, 59(1):52, 1987.

[53] Wilks, S., Kruer, W., Tabak, M., and Langdon, A. Absorption of ultra-intense laser pulses. *Phys. Rev. Lett*, 69(9):1383, 1992.

[54] Pukhov, A. Three-dimensional simulations of ion acceleration from a foil irradiated by a short-pulse laser. *Phys. Rev. Lett*, 86(16):3562, 2001.

[55] Mackinnon, A., Sentoku, Y., Patel, P., Price, D., Hatchett, S., Key, M., Andersen, C., Snavely, R., and Freeman, R. Enhancement of proton acceleration by hot-electron recirculation in thin foils irradiated by ultraintense laser pulses. *Phys. Rev. Lett*, 88(21):215006, 2002.

[56] Roth, M., Blazevic, A., Geissel, M., Schlegel, T., Cowan, T., Allen, M., Gauthier, J.-C., Audebert, P., Fuchs, J., Meyer-ter Vehn, J., et al. Energetic ions generated by laser pulses: A detailed study on target properties. *Physical Review Special Topics-Accelerators and Beams*, 5(6):061301, 2002.

[57] Mora, P. Plasma expansion into a vacuum. *Phys. Rev. Lett*, 90(18):185002, 2003.

[58] Fuchs, J., Antici, P., d'Humières, E., Lefebvre, E., Borghesi, M., Brambrink, E., Cecchetti, C., Kaluza, M., Malka, V., Manclossi, M., et al. Laser-driven proton scaling laws and new paths towards energy increase. *Nature physics*, 2(1):48–54, 2006.

[59] Mora, P. Thin-foil expansion into a vacuum. *Phys. Rev. E*, 72(5):056401, 2005.

[60] Schreiber, J., Bell, F., Grüner, F., Schramm, U., Geissler, M., Schnürer, M., Ter-Avetisyan, S., Hegelich, B. M., Cobble, J., Brambrink, E., et al. Analytical model for ion acceleration by high-intensity laser pulses. *Phys. Rev. Lett*, 97(4):045005, 2006.

[61] Hegelich, M., Karsch, S., Pretzler, G., Habs, D., Witte, K., Guenther, W., Allen, M., Blazevic, A., Fuchs, J., Gauthier, J., et al. Mev ion jets from short-pulse-laser interaction with thin foils. *Phys. Rev. Lett*, 89(8):085002, 2002.

[62] Cowan, T., Fuchs, J., Ruhl, H., Kemp, A., Audebert, P., Roth, M., Stephens, R., Barton, I., Blazevic, A., Brambrink, E., et al. Ultralow emittance, multi-mev proton beams from a laser virtual-cathode plasma accelerator. *Phys. Rev. Lett*, 92(20):204801, 2004.

[63] Mckenna, P., Lindau, F., Lundh, O., Carroll, D., Clarke, R., Ledingham, K., McCanny, T., Neely, D., Robinson, A., Robson, L., et al. Low-and medium-mass ion acceleration driven by petawatt laser plasma interactions. *Plasma Physics and Controlled Fusion*, 49(12B):B223, 2007.

[64] Robson, L., Simpson, P., Clarke, R. J., Ledingham, K. W., Lindau, F., Lundh, O., McCanny, T., Mora, P., Neely, D., Wahlström, C.-G., et al. Scaling of proton acceleration driven by petawatt-laser–plasma interactions. *Nature physics*, 3(1):58–62, 2007.

[65] McKenna, P., Carroll, D., Lundh, O., Nürnberg, F., Markey, K., Bandyopadhyay, S., Batani, D., Evans, R., Jafer, R., Kar, S., et al. Effects of front surface plasma expansion on proton acceleration in ultraintense laser irradiation of foil targets. *Laser Part. Beams*, 26(4):591–596, 2008.

[66] Borghesi, M., Mackinnon, A., Campbell, D. H., Hicks, D., Kar, S., Patel, P. K., Price, D., Romagnani, L., Schiavi, A., and Willi, O. Multi-mev proton source investigations in ultraintense laser-foil interactions. *Phys. Rev. Lett*, 92(5):055003, 2004.

[67] Allen, M., Patel, P. K., Mackinnon, A., Price, D., Wilks, S., and Morse, E. Direct experimental evidence of back-surface ion acceleration from laser-irradiated gold foils. *Phys. Rev. Lett*, 93(26):265004, 2004.

[68] Kaluza, M., Schreiber, J., Santala, M. I., Tsakiris, G. D., Eidmann, K., Meyer-ter Vehn, J., and Witte, K. J. Influence of the laser prepulse on proton acceleration in thin-foil experiments. *Phys. Rev. Lett*, 93(4):045003, 2004.

[69] Mackinnon, A., Borghesi, M., Hatchett, S., Key, M., Patel, P., Campbell, H., Schiavi, A., Snavely, R., Wilks, S., and Willi, O. Effect of plasma scale length on multi-mev proton production by intense laser pulses. *Phys. Rev. Lett*, 86(9):1769, 2001.

[70] Esirkepov, T., Borghesi, M., Bulanov, S., Mourou, G., and Tajima, T. Highly efficient relativistic-ion generation in the laser-piston regime. *Phys. Rev. Lett*, 92(17):175003, 2004.

[71] Macchi, A., Cattani, F., Liseykina, T. V., and Cornolti, F. Laser acceleration of ion bunches at the front surface of overdense plasmas. *Phys. Rev. Lett.*, 94(16):165003, 2005.

[72] Zhang, X., Shen, B., Li, X., Jin, Z., Wang, F., and Wen, M. Efficient gev ion generation by ultraintense circularly polarized laser pulse. *Phys. Plasmas*, 14(12):123108, 2007.

[73] Liseikina, T. and Macchi, A. Features of ion acceleration by circularly polarized laser pulses. *Applied physics letters*, 91(17):171502, 2007.

[74] Tamburini, M., Liseykina, T., Pegoraro, F., and Macchi, A. Radiation-pressure-dominant acceleration: Polarization and radiation reaction effects and energy increase in three-dimensional simulations. *Phys. Rev. E*, 85(1):016407, 2012.

[75] Denavit, J. Absorption of high-intensity subpicosecond lasers on solid density targets. *Phys. Rev. Lett.*, 69(21):3052, 1992.

[76] Robinson, A., Gibbon, P., Zepf, M., Kar, S., Evans, R., and Bellei, C. Relativistically correct hole-boring and ion acceleration by circularly polarized laser pulses. *Plasma Physics and Controlled Fusion*, 51(2):024004, 2009.

[77] Schlegel, T., Naumova, N., Tikhonchuk, V., Labaune, C., Sokolov, I., and Mourou, G. Relativistic laser piston model: Ponderomotive ion acceleration in dense plasmas using ultraintense laser pulses. *Phys. Plasmas*, 16(8):083103, 2009.

[78] Cattani, F., Kim, A., Anderson, D., and Lisak, M. Threshold of induced transparency in the relativistic interaction of an electromagnetic wave with overdense plasmas. *Phys. Rev. E*, 62(1):1234, 2000.

[79] Robinson, A. Production of high energy protons with hole-boring radiation pressure acceleration. *Phys. Plasmas*, 18(5):056701, 2011.

[80] Robinson, A., Zepf, M., Kar, S., Evans, R., and Bellei, C. Radiation pressure acceleration of thin foils with circularly polarized laser pulses. *New J. Phys.*, 10(1):013021, 2008.

[81] Forslund, D. and Shonk, C. Formation and structure of electrostatic collisionless shocks. *Phys. Rev. Lett*, 25(25):1699, 1970.

[82] Haberberger, D., Tochitsky, S., Fiuza, F., Gong, C., Fonseca, R. A., Silva, L. O., Mori, W. B., and Joshi, C. Collisionless shocks in laser-produced plasma generate monoenergetic high-energy proton beams. *Nature Physics*, 8(1):95–99, 2012.

[83] Silva, L. O., Marti, M., Davies, J. R., Fonseca, R. A., Ren, C., Tsung, F. S., and Mori, W. B. Proton shock acceleration in laser-plasma interactions. *Phys. Rev. Lett.*, 92(1):015002, 2004.

[84] d'Humières, E., Lefebvre, E., Gremillet, L., and Malka, V. Proton acceleration mechanisms in high-intensity laser interaction with thin foils. *Phys. Plasmas*, 12(6):062704, 2005.

[85] Chen, M., Sheng, Z.-M., Dong, Q.-L., He, M.-Q., Li, Y.-T., Bari, M. A., and Zhang, J. Collisionless electrostatic shock generation and ion acceleration by ultraintense laser pulses in overdense plasmas. *Phys. Plasmas*, 14(5):053102, 2007.

[86] Pak, A., Kerr, S., Lemos, N., Link, A., Patel, P., Albert, F., Divol, L., Pollock, B., Haberberger, D., Froula, D., et al. Collisionless shock acceleration of narrow energy spread ion beams from mixed species plasmas using 1 μ m lasers. *Physical Review Accelerators and Beams*, 21(10):103401, 2018.

[87] Macchi, A., Nindrayog, A. S., and Pegoraro, F. Solitary versus shock wave acceleration in laser-plasma interactions. *Phys. Rev. E*, 85(4):046402, 2012.

[88] Yin, L., Albright, B., Hegelich, B., and Fernández, J. Gev laser ion acceleration from ultrathin targets: The laser break-out afterburner. *Laser Part. Beams*, 24(2):291–298, 2006.

[89] Yin, L., Albright, B., Hegelich, B., Bowers, K. J., Flippo, K., Kwan, T., and Fernández, J. Monoenergetic and gev ion acceleration from the laser breakout afterburner using ultrathin targets. *Phys. Plasmas*, 14(5):056706, 2007.

[90] Albright, B., Yin, L., Bowers, K. J., Hegelich, B., Flippo, K., Kwan, T., and Fernandez, J. Relativistic buneman instability in the laser breakout afterburner. *Phys. Plasmas*, 14(9):094502, 2007.

[91] Buneman, O. Instability, turbulence, and conductivity in current-carrying plasma. *Phys. Rev. Lett*, 1(1):8, 1958.

[92] Di Lucchio, L., Andreev, A. A., and Gibbon, P. Ion acceleration by intense, few-cycle laser pulses with nanodroplets. *Phys. Plasmas*, 22(5):053114, 2015.

[93] Ostermayr, T. *Relativistically Intense Laser–Microplasma Interactions*. Springer, 2019.

[94] Bulanov, S., Brantov, A., Bychenkov, V. Y., Chvykov, V., Kalinchenko, G., Matsuoka, T., Rousseau, P., Reed, S., Yanovsky, V., Litzenberg, D., et al. Accelerating monoenergetic protons from ultrathin foils by flat-top laser pulses in the directed-coulomb-explosion regime. *Phys. Rev. E*, 78(2):026412, 2008.

[95] Limpouch, J., Psikal, J., Andreev, A., Platonov, K. Y., and Kawata, S. Enhanced laser ion acceleration from mass-limited targets. *Laser Part. Beams*, 26(2):225–234, 2008.

[96] Buffechoux, S., Psikal, J., Nakatsutsumi, M., Romagnani, L., Andreev, A., Zeil, K., Amin, M., Antici, P., Burris-Mog, T., Compant-La-Fontaine, A., et al. Hot electrons transverse refluxing in ultraintense laser-solid interactions. *Phys. Rev. Lett*, 105(1):015005, 2010.

[97] Kluge, T., Enghardt, W., Kraft, S., Schramm, U., Zeil, K., Cowan, T., and Bussmann, M. Enhanced laser ion acceleration from mass-limited foils. *Phys. Plasmas*, 17(12):123103, 2010.

[98] Zeil, K., Metzkes, J., Kluge, T., Bussmann, M., Cowan, T., Kraft, S., Sauerbrey, R., Schmidt, B., Zier, M., and Schramm, U. Robust energy enhancement of ultrashort pulse laser accelerated protons from reduced mass targets. *Plasma Physics and Controlled Fusion*, 56(8):084004, 2014.

[99] Zheng, J., Sheng, Z.-M., Peng, X.-Y., and Zhang, J. Energetic electrons and protons generated from the interaction of ultrashort laser pulses with microdroplet plasmas. *Phys. Plasmas*, 12(11):113105, 2005.

[100] Henig, A., Kiefer, D., Geissler, M., Rykovanov, S. G., Ramis, R., Hörlein, R., Osterhoff, J., Major, Z., Veisz, L., Karsch, S., et al. Laser-driven shock acceleration of ion beams from spherical mass-limited targets. *Phys. Rev. Lett*, 102(9):095002, 2009.

[101] Sokollik, T., Paasch-Colberg, T., Gorling, K., Eichmann, U., Schnürer, M., Steinke, S., Nickles, P., Andreev, A., and Sandner, W. Laser-driven ion acceleration using isolated mass-limited spheres. *New J. Phys.*, 12(11):113013, 2010.

[102] Ostermayr, T. M., Haffa, D., Hilz, P., Pauw, V., Allinger, K., Bamberg, K.-U., Böhl, P., Bömer, C., Bolton, P., Deutschmann, F.,

et al. Proton acceleration by irradiation of isolated spheres with an intense laser pulse. *Phys. Rev. E*, 94(3):033208, 2016.

[103] Hilz, P., Ostermayr, T., Huebl, A., Bagnoud, V., Borm, B., Bussmann, M., Gallei, M., Gebhard, J., Haffa, D., Hartmann, J., et al. Isolated proton bunch acceleration by a petawatt laser pulse. *Nature communications*, 9(1):1–9, 2018.

[104] Bhagawati, A., Kuri, D. K., and Das, N. Proton acceleration due to laser plasma interactions from mass-limited spherical targets. *Phys. Plasmas*, 26(9):093106, 2019.

[105] Okada, T., Andreev, A., Mikado, Y., and Okubo, K. Energetic proton acceleration and bunch generation by ultraintense laser pulses on the surface of thin plasma targets. *Phys. Rev. E*, 74(2):026401, 2006.

[106] Liu, J., Chen, M., Sheng, Z., Liu, C., Mori, W., Zhang, J., et al. Stable laser-produced quasimonoenergetic proton beams from interactive laser and target shaping. *Physical Review Special Topics-Accelerators and Beams*, 16(12):121301, 2013.

[107] Chen, M., Yu, T.-P., Pukhov, A., and Sheng, Z.-M. Target shape effects on monoenergetic gev proton acceleration. *New J. Phys.*, 12(4):045004, 2010.

[108] Wang, H., Yan, X., Lu, Y., Zheng, F., Guo, Z., Ma, W., He, X., Tajima, T., Habs, D., and Chen, J. Autofocused, enhanced proton acceleration from a nanometer-scale bulged foil. *Phys. Plasmas*, 17(11):113111, 2010.

[109] Zou, D., Zhuo, H., Yu, T., Wu, H., Yang, X., Shao, F., Ma, Y., Yin, Y., and Ge, Z. Enhanced laser-radiation-pressure-driven proton acceleration by moving focusing electric-fields in a foil-in-cone target. *Phys. Plasmas*, 22(2):023109, 2015.

[110] Zou, D., Zhuo, H., Yang, X., Yu, T., Shao, F., and Pukhov, A. Control of target-normal-sheath-accelerated protons from a guiding cone. *Phys. Plasmas*, 22(6):063103, 2015.

[111] Gaillard, S., Kluge, T., Flippo, K., Bussmann, M., Gall, B., Lockard, T., Geissel, M., Offermann, D., Schollmeier, M., Sentoku, Y., et al. Increased laser-accelerated proton energies via direct laser-light-pressure acceleration of electrons in microcone targets. *Phys. Plasmas*, 18(5):056710, 2011.

[112] Birdsall, C. K. and Langdon, A. B. *Plasma physics via computer simulation*. CRC press, 2018.

[113] Yee, K. Numerical solution of initial boundary value problems involving maxwell's equations in isotropic media. *IEEE Transactions on antennas and propagation*, 14(3):302–307, 1966.